

Chapter 4

The Evolution of Dust Formation in SN 1987A

On 23 February 1987, a star died in an explosion that would inform our understanding of core-collapse supernovae for decades to come. SN 1987A is uniquely important to the study of supernovae. At only 50kpc away in the Large Magellanic Cloud (LMC) and as the brightest supernova to be observed since SN 1604 (Kepler), it has provided an unprecedented opportunity for studying every aspect of supernovae. Since its discovery by Ian Shelton and Oscar Duhalde at Las Campanas, Chile (Kunkel et al. 1987), SN 1987A has been continuously observed across the entire wavelength range providing astronomers with a wealth of data and discoveries.

SN 1987A was the first supernova to be detected via the emission of neutrinos. Hours before the visible light from SN 1987A reached Earth, 19 neutrinos were simultaneously detected in various locations across the globe confirming the core-collapse theory of supernovae (Bionta et al. 1987; Hirata et al. 1987). However, the neutron star that is expected to have resulted from this collapse has yet to be detected. Various theories exist for this non-detection such as the possibility that a black hole formed instead of a neutron star or that dust is obscuring our view.

The detection of neutrinos in combination with the presence of hydrogen lines in the early spectra resulted in the classification of SN 1987A as a Type II supernova. However, SN 1987A was unusually dim compared to other Type II SNe and brightened very quickly,



Figure 4.1. SN 1987A in the Large Magellanic Cloud. The three-colour image is composed of several pictures of the region taken with the Wide Field and Planetary Cameras on the Hubble Space Telescope between September 1994 and July 1997. Image courtesy of NASA, ESA, and The Hubble Heritage Team (STScI/AURA).

its magnitude increasing by a factor of 100 in just three hours compared to a normal timeframe of several days. SN 1987A exhibited a number of other somewhat unusual features. Broad lines detected in the very early spectra indicated expansion velocities of up to $30,000 \text{ km s}^{-1}$, much faster than the typical $15,000 \text{ km s}^{-1}$. The colour evolution of the object was also faster than expected. These atypical properties suggested that the progenitor star was more compact than the red supergiants that normally give rise to Type II SNe. In fact, four days after the initial detection of SN 1987A, the progenitor star was identified as the blue supergiant Sanduleak -69° 202 confirming this theory (Sonneborn et al. 1987). These distinctive features, in combination with a plateauing light curve, led to the final classification of SN 1987A as a peculiar Type II-P supernova.

After the initial flash of ionising radiation in the first few hours (Ensmann & Burrows 1992), the expanding debris of SN 1987A cooled rapidly dropping from 14,000K to 6,000K

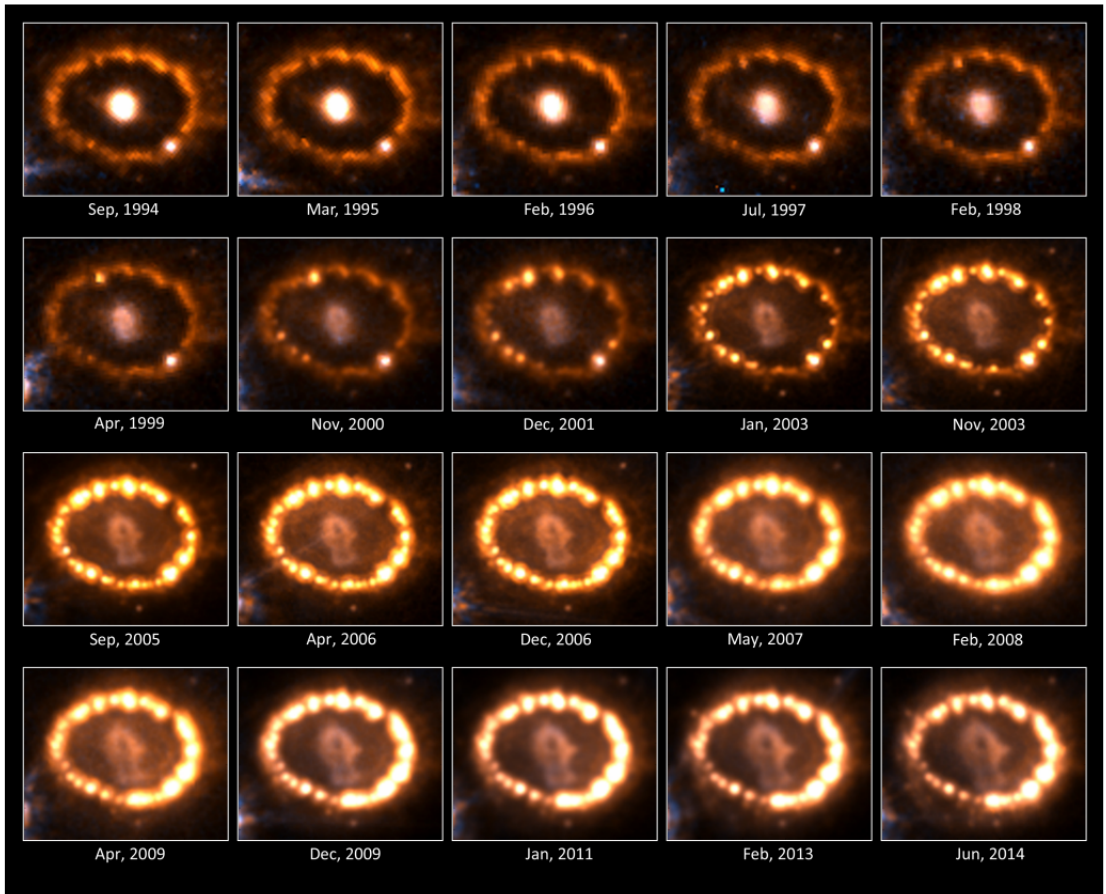


Figure 4.2. Evolution of the ring collision from 1994 to 2014 from a combination of HST B- and R- band images. The brightness of the ring has been reduced by a factor of 20 by applying a mask to the images making it possible to see the morphology of the ring at the same time as the faint ejecta. The image is taken from (Fransson et al. 2015).

between the first and tenth days after outburst (Kirshner et al. 1987) before eventually stabilising at around 5,500K. By just four months after outburst, the debris were transparent in the optical and IR (McCray 1993). The ejecta spectrum was dominated by emission lines, often exhibiting P-Cygni profiles, rising from a blackbody continuum. Numerous hydrogen, calcium and sodium lines could be seen in the optical as well as a rich spectrum of IR emission lines from other heavy elements.

The forward shock continued to propagate through the ejecta and by the mid 1990s reached the innermost of the beautiful and complex system of rings that are observed around SN 1987A (see Figure 4.1). The rings were most likely caused by an ejection of mass following a binary merger some 20,000 years before SN 1987A exploded (Morris & Podsiadlowski 2005; Fitzpatrick et al. 2013). This merger also likely explains the surprising

blue colour of the progenitor star. A series of images of the equatorial ring (ER) taken using the Hubble Space Telescope (HST) clearly show the appearance of “hot spots” as the dense material is shock-ionised on impact with the forward shock (see Figure 4.2). The interaction of the forward shock with the ER has precipitated a strong reverse shock that is now travelling back through the ejected material (Fransson et al. 2013). The illumination of the outer parts of the ejecta by the reverse shock is visible in spectra taken at later epochs as faster regions became more dominant in line profiles making them appear broader. It has been suggested that this point in SN 1987A’s evolution marks its transition to a remnant (McCray 2003).

The ionisation and heating of the ejecta of the supernova is caused by gamma rays that result from the decay of ^{56}Co , ^{57}Co and ^{44}Ti (with half lives of 77.3 days, 272 days and 59 years respectively (Ahmad et al. 2002)). The gamma rays Compton scatter off electrons that are often bound causing the production of fast, primary photoelectrons. These primary electrons go on to impact atoms causing further ionisations and excitations. A population of secondary electrons is thus produced. Recombinations and de-excitations result in the emission of monochromatic photons. These emission lines are then broadened thermally and via the large bulk velocity of the emitting medium. I present models of these optical and IR emission line profiles from SN 1987A throughout this chapter. The ionisation state of the ejecta of SN 1987A is thought to reach a period of stability known as the “freeze-out” when a balance is reached between the recombination and ionisation rates (Danziger et al. 1991b; Kozma & Fransson 1998a; Fransson et al. 2013). This is discussed in further detail later in this chapter as it has relevance to the evolution of the shapes of the line profiles.

A full review of SN 1987A in all its glory would likely extend to many dozen of pages and so in the following paragraphs I will focus only on those facets of the history of SN 1987A that relate to the formation of dust in its ejecta. For extensive reviews covering the progenitor, the explosion mechanism, the dynamics and geometry, the light curves and spectral evolution, the thermodynamics, the chemistry and the circumstellar ring system I refer the reader to Arnett et al. (1989), McCray (1993) and McCray (2003). A comprehensive review of SN 1987A by Richard McCray encompassing its later evolution is due to be published next year (McCray & Fransson 2016).

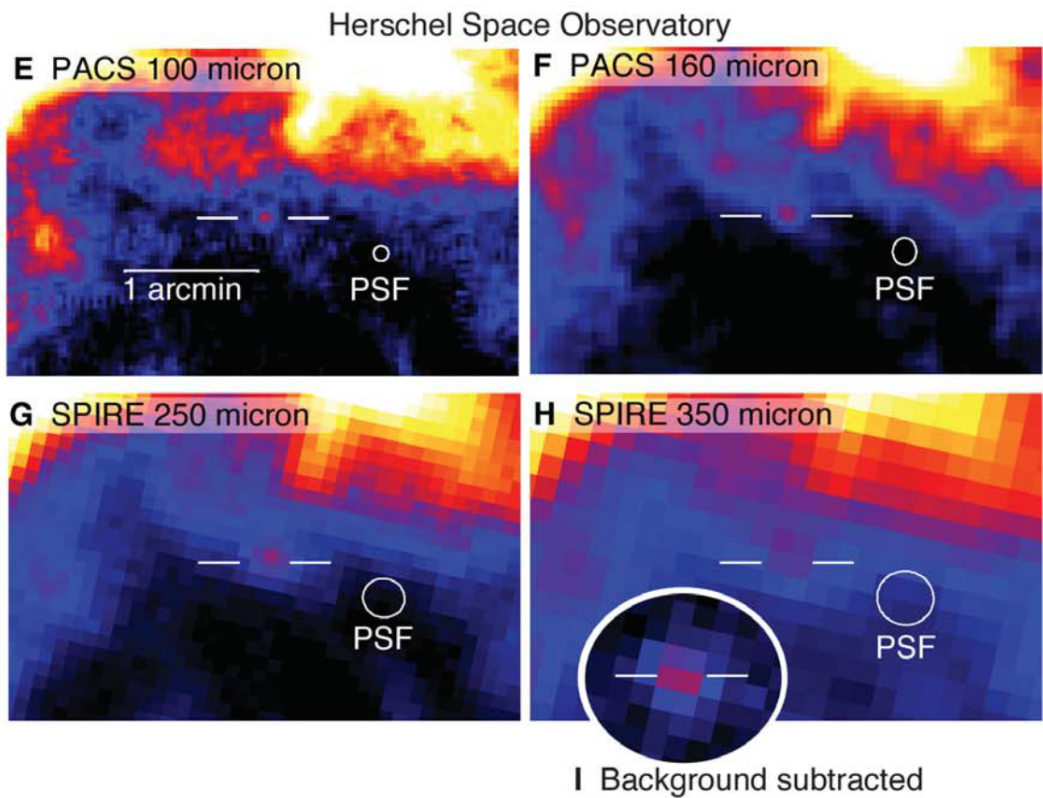


Figure 4.3. *Herschel* images of SN 1987A. Image taken from (Matsuura et al. 2011).

4.1 10,000 Days of Dust

SN 1987A is the first and only supernova to have had the formation of dust in its ejecta traced via all three observable signatures described in Section 1.2.4 (Bouchet & Danziger 2014). Before dust was observed, its formation in the ejecta of SN 1987A was predicted. Gehrz & Ney (1987) recognized that conditions in the cooling ejecta would eventually reach temperatures and densities appropriate for dust formation to occur. They predicted that the onset of dust formation would occur at around days 240-300. This idea was expanded upon by Dwek (1988) who estimated that dust would begin to form slightly later at around day 400.

The first indications of dust in the ejecta of SN 1987A appeared at around day 350 with the emergence of continuum radiation in the IR longward of $5\mu\text{m}$ (Meikle et al. 1993). This had become prominent by day 550 (Roche et al. 1993; Wooden et al. 1993). It was suggested by some that this excess IR emission was the result of a light echo reflecting off the circumstellar material (Roche et al. 1989). However, at around day 530, the optical

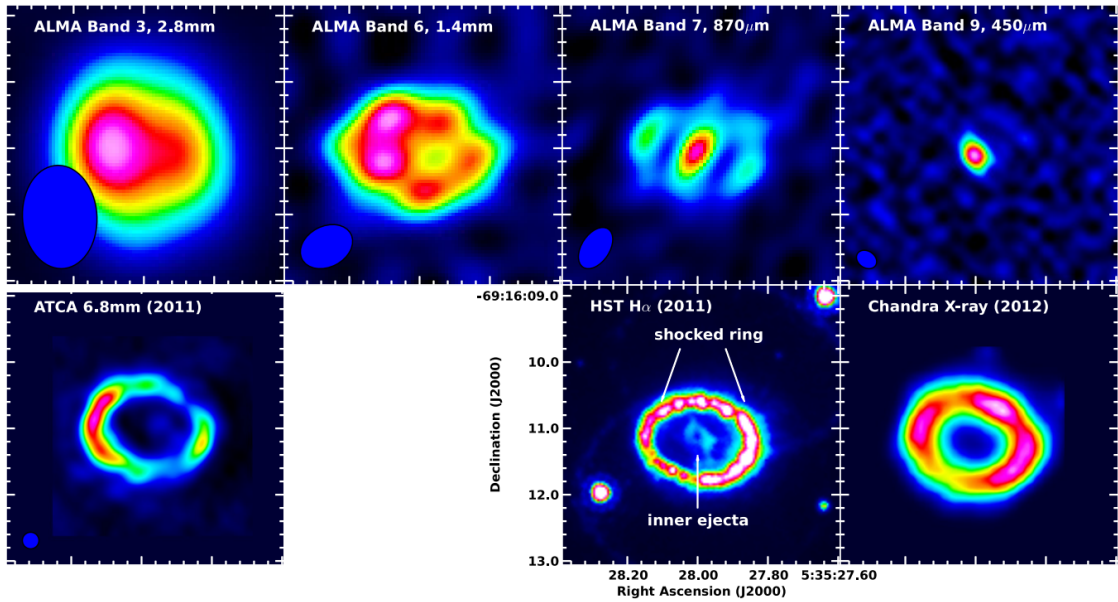


Figure 4.4. ALMA, ATCA, HST and Chandra images of SN 1987A showing the location of the dust in the inner ejecta. The image is taken from (Indebetouw et al. 2014). Inset HST image courtesy of R. Kirshner and the SAINTS collaboration (also see Larsson et al. (2013)) and the inset Chandra X-ray image is from Helder et al. (2013).

luminosity suddenly started dropping more rapidly than it had done previously. The IR luminosity started to increase, compensating for the drop in the optical and ensuring that the bolometric light curve continued to follow the same trajectory (Suntzeff et al. 1991; Whitelock et al. 1991). At the same time it was observed that the peaks of several emission lines in the optical and IR had become shifted towards the blue indicating that the dust was indeed within the supernova envelope itself (Danziger et al. 1991a,b; Meikle et al. 1991, 1993; Suntzeff et al. 1991; Hanuschik et al. 1993). It was Leon Lucy and collaborators who first suggested that the presence of blue-shifted line profiles may indicate dust formation in the ejecta of supernovae and they even went as far as producing some models to illustrate the effects. In 1989, they used this method for the first time to estimate the dust mass in the ejecta of SN 1987A ($10^{-6}M_{\odot} - 10^{-4}M_{\odot}$) (Lucy et al. 1989, 1991).

After the intensive monitoring of SN 1987A in the MIR, there was something of a gap in observations. By the mid 1990s SN 1987A had faded and could no longer be detected in the MIR with current instruments. It was not until 2004 that new instruments at the Gemini South telescope and at the Very Large Telescope allowed for the resumption of observations at these wavelengths. The first resolved detection of the central ejecta was reported in 2004 by Bouchet et al. (2004) who observed the object at $10\mu\text{m}$ and at $20\mu\text{m}$.

They reported a dust mass estimate of $10^{-4}M_{\odot} - 2 \times 10^{-3}M_{\odot}$ for the dust in the ejecta with an estimated temperature of $90K < T < 100K$. They concluded that CCSNe could potentially be a significant source of dust in the universe but could not solely account for the masses seen at high redshifts (see Chapter 1). Subsequent observations continued to detect this faint MIR emission right up to the present day (Dwek et al. 2010; Bouchet & Danziger 2014) whilst radiative transfer models of the SEDs continued to find dust masses of the order of $10^{-4} - 10^{-3}M_{\odot}$ (Ercolano et al. 2007).

For many years it was assumed that only a small mass of dust, possibly as much as a few $\times 10^{-3}M_{\odot}$, had formed in the ejecta of SN 1987A within the first 1000 days. It was not until the first *Herschel* observations of SN 1987A that the picture suddenly changed. SN 1987A had not been chosen as a target for the *Herschel* mission as it was believed that it would not be detectable at far-IR and sub-mm wavelengths. However, in 2010, whilst *Herschel* was performing a survey of the LMC as a part of the HERITAGE survey (Meixner et al. 2013), an unexpectedly strong signal was detected in the same region as SN 1987A. In 2011, Matsuura et al. (2011) published the first detections of the SN 1987A system at long wavelengths (100, 160, 250 and 350 μ m presented in Figure 4.3). These observations revealed the presence of a massive reservoir ($0.4 - 0.7 M_{\odot}$) of cold dust ($17K < T < 23K$) that they claimed was located in the ejecta. *Herschel* did not have the angular resolution to determine the location of the emitting dust and as a result there was much contention over this assertion with many claiming that the detection was of pre-existing dust located in the circumstellar material (Bouchet & Danziger 2014). However, follow-up observations of SN 1987A with the Atacama Large Millimetre Array (ALMA) published by Indebetouw et al. (2014) resolved the SN-ring system and revealed the location of the dust to be entirely within the ejecta (see Figure 4.4). Further *Herschel* observations corroborated the large estimated dust masses (Matsuura et al. 2015). These dust mass estimates were all based on fitting dust spectral energy distributions (SEDs) that peaked at far-IR wavelengths.

The majority of the dust in the ejecta of SN 1987A is located centrally and as such has not yet encountered the reverse shock that is propagating back towards it. Whilst it is now clear that very large masses of dust have indeed formed in the ejecta of SN 1987A, it remains unclear whether the dust will survive the passage of the reverse shock. The composition of the dust and the size of the grains are crucial to understanding how much of the dust that has formed will actually be deposited into the ISM in the future. Further ob-

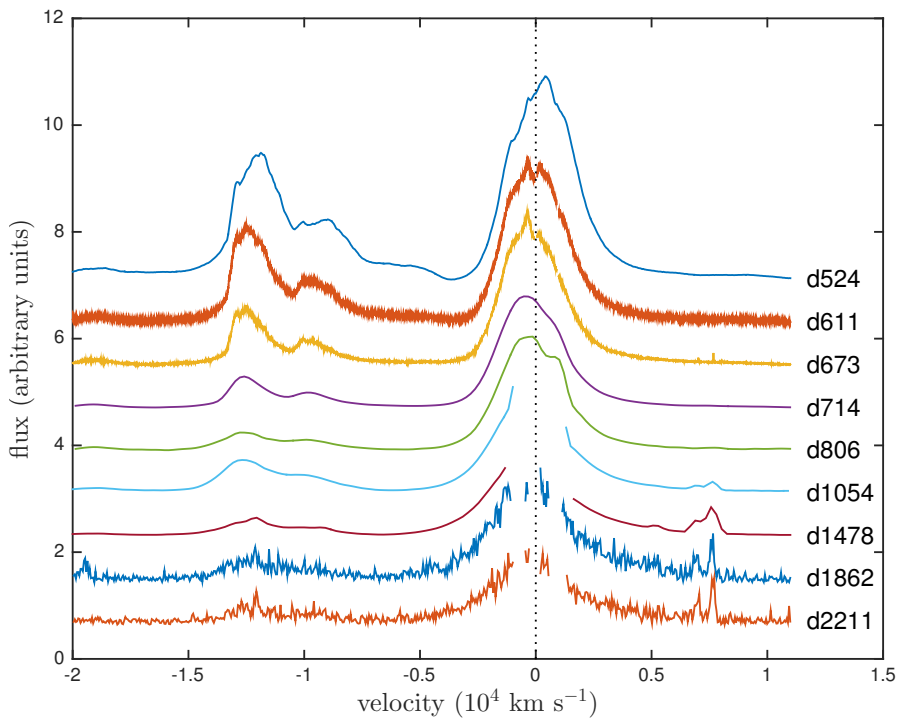


Figure 4.5. Archival data showing the evolution of the H α and [O I] line profiles from SN 1987A at the earlier of the epochs considered. The spectral gaps at the last two epochs correspond to where narrow line emission from the equatorial ring has been removed. The spectra have been continuum-subtracted and offsets have been applied for display purposes.

servations and analyses of the dust mass present in the ejecta are crucial to understanding how much dust is actually contributed to the ISM from CCSNe.

The *Herschel* mission ended in 2013 and there is now likely to be a long wait for far-IR facilities with comparable or better sensitivities than *Herschel* to become available. The method of SED fitting is therefore unhelpful until other telescopes come into operation. This provides a strong incentive to make use of alternative methods to estimate the dust masses that form in supernova ejecta. Virtually no analysis of the shapes of the line profiles in SN 1987A has been performed before. With such a large database of spectral observations available, SN 1987A provides the perfect opportunity to assess the evolution of the formation of dust in the ejecta of CCSNe.

In this chapter, I present a number of models of line profiles of SN 1987A. I have collated optical spectra from the archives of four different telescopes in order to study the effects of dust formation on the H α line and on the [O I] $\lambda\lambda 6300, 6363$ Å doublet. I have modelled epochs spanning a range of approximately 8 years from the first indications

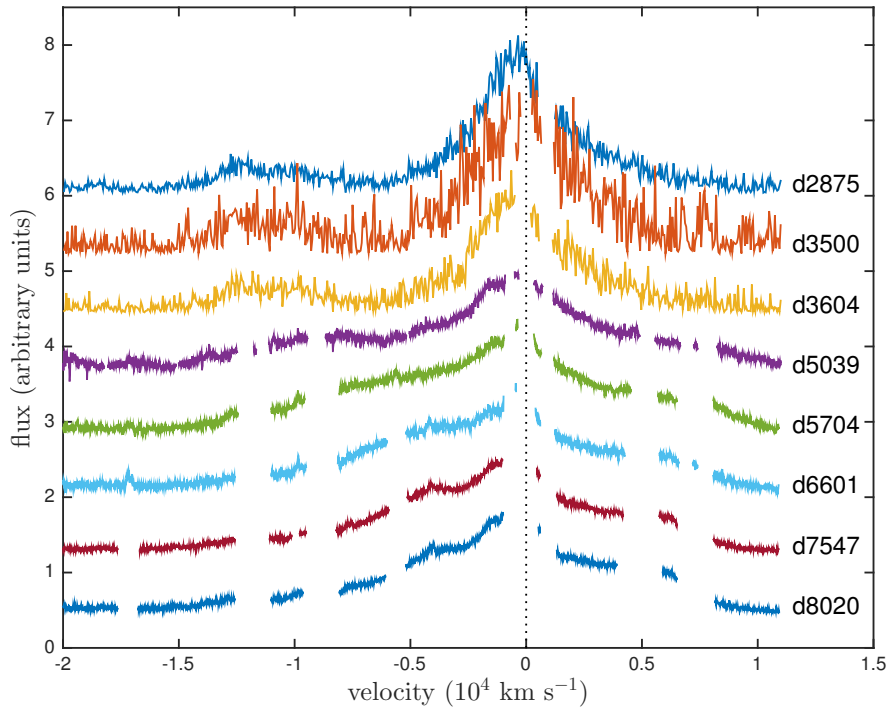


Figure 4.6. Archival data showing the evolution of the H α line profile from SN 1987A at the later epochs. The spectral gaps correspond to where narrow line emission from the ER has been removed. The spectra have been continuum-subtracted and offsets applied for display purposes.

of blue-shifting in the H α line between days 600-700, using both smooth and clumped geometries. I compare my derived dust masses to those obtained by Wesson et al. (2015) (hereafter W15) and Dwek & Arendt (2015) (hereafter DA15) and consider the implied dust formation rate.

In Section 4.2, I detail the observed spectra that I used for my modelling and I present my modelling of the H α and [O I] $\lambda\lambda 6300, 6363$ Å lines in Section 4.3. Finally, I discuss my findings in Section 4.4.

4.2 Spectral Observations of SN 1987A

SN 1987A has been the most intensively observed supernova in history, with an abundance of both spectral and photometric data available to model. From the archives of a number of different telescopes I have collated optical spectra acquired over a wide range of epochs. At the earlier epochs I use spectra obtained by the Anglo-Australian Telescope (AAT) and the Cerro Tololo Inter-American Observatory (CTIO) and at later epochs I use spectra

Table 4.1. Details of the archival data for SN 1987A.

Date	Age (days)	Telescope	Inst	λ_{min} (Å)	λ_{max} (Å)	Res. (Å)	Res. Power	Reference
31 Jul 1988	524	AAT	FORS	5500	10190	20		Spyromilio et al. (1991)
26 Oct 1988	611	AAT	UCLES	6011	7336	30000		Hanuschik et al. (1993; Spyromilio et al. (1993))
27 Dec 1988	673	AAT	UCLES	5702	10190	30000		Hanuschik et al. (1993; Spyromilio et al. (1993))
06 Feb 1989	714	CTIO-1.5m	Cass.	6420	10380	16		Phillips et al. (1990)
09 May 1989	806	CTIO-1.5m	Cass.	6430	10330	16		Phillips et al. (1990)
12 Jan 1990	1054	CTIO-4m	RC	3565	10000	11		Suntzeff et al. (1991)
12 Mar 1991	1478	CTIO-4m	RC	3245	9175	11		
30 Mar 1992	1862	HST	STIS	4569	6818	4.4		Wang et al. (1996)
14 Mar 1993	2211	HST	STIS	4569	6818	4.4		Wang et al. (1996)
07 Jan 1995	2875	HST	STIS	4569	6818	4.4		Chugai et al. (1997)
23 Sep 1996	3500	HST	STIS	4569	6818	4.4		
05 Jan 1997	3604	HST	STIS	4569	6818	4.4		
10 Dec 2000	5039	VLT	UVES	4760	6840	50000		Grönningsson et al. (2006, 2007)
06 Oct 2002	5704	VLT	UVES	4760	6840	50000		Grönningsson et al. (2006, 2007, 2008)
21 Mar 2005	6601	VLT	UVES	4760	6840	50000		Grönningsson et al. (2006, 2007)
23 Oct 2007	7547	VLT	UVES	4760	6840	50000		Grönningsson et al. (2007)
07 Feb 2009	8020	VLT	UVES	4800	6800	50000		Tziampatzis et al. (2010)

from the archives of the Hubble Space Telescope (HST) and the Very Large Telescope (VLT). An explosion date of 23 February 1987 is adopted throughout and epochs are measured relative to this date. Full details of all observations may be found in Table 4.1. The spectral resolutions of the grating spectrograph observations are listed in column 7, while column 8 lists the spectral resolving powers of the echelle spectrograph observations.

Wavelength ranges encompassing the H α line and [O I] $\lambda\lambda 6300, 6363$ Å doublet were selected in order to trace their evolution from day 524, near the time of the first indications of dust formation (Wooden et al. 1993), to day 8020, near the current era. Optical spectroscopy obtained at the AAT using the Faint Object Red Spectrograph (FORS) during the first two years after outburst was kindly supplied by Dr Raylee Stathakis (Spyromilio et al. 1991, 1993; Hanuschik et al. 1993) and optical spectra from the CTIO were donated by Dr Mark Phillips (Suntzeff et al. 1991).

The evolution of the H α and [O I] line profiles is presented in Figures 4.5 and 4.6. At later epochs, the broad H α profile emitted by the ejecta becomes contaminated by narrow line emission from the ER. These lines have been removed for the purposes of modelling the broad line. A continuum fit has been subtracted from each spectrum and a velocity correction has been applied for a recession velocity of 287 km s $^{-1}$ (Gröningsson et al. 2008).

4.2.1 Contamination of the H α profiles

The H α profile at day 714 exhibits a very slight inflection visible at $V \approx +900$ km s $^{-1}$. By day 806, this slight inflection has developed into a noticeable shoulder in the line profile of H α (see Figure 4.9).

Although these features are similar in nature to features produced by dust absorption in the flat-topped region (as discussed in Section 3.2.5), I conclude that this shoulder is an early appearance of the unresolved [N II] $\lambda 6583$ Å line from the ER (Kozma & Fransson 1998b). Unresolved nebular [N II] lines at $\lambda = 6583$ Å and $\lambda = 6548$ Å either side of the H α rest frame velocity at 6563 Å are certainly seen by day 1054 and have to be removed in order to consider the evolution of the broad H α profile (see Figure 4.5). I do not remove this potential contaminant at earlier epochs but try to fit the broad line profiles around it.

By day 1054, all three of the narrow nebular lines are strong. They remain unresolved in the low spectral resolution CTIO data at days 1054 and 1478 and therefore contaminate

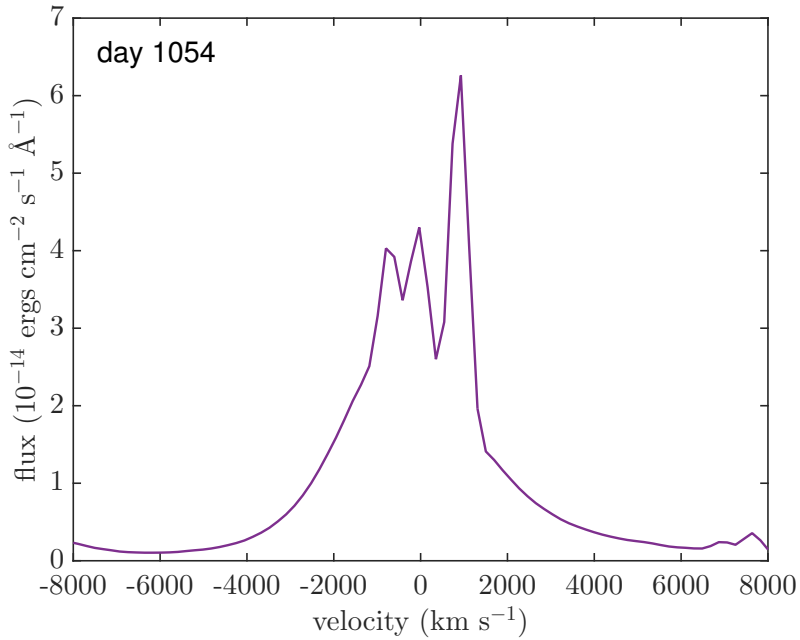


Figure 4.7. The low resolution H α line profile from SN 1987A observed at the CTIO on day 1054. The unresolved narrow nebular [N II] lines at $\lambda = 6583 \text{ \AA}$ and $\lambda = 6548 \text{ \AA}$ and the narrow nebular H α line at $\lambda = 6563 \text{ \AA}$ can be clearly seen.

the entire central region of the H α line profile (see Figure 4.7). Their presence renders two CTIO H α profiles from days 1054 and 1478 unusable for modelling purposes. The HST and VLT H α profiles at later epochs (≥ 1862 days) have a higher spectral resolution and it was therefore easier to remove the narrower [N II] and H α lines from the broad H α profiles (for example Figures 4.5 and 4.6). Although this does remove a potentially informative section of the profile ($+500 \text{ km s}^{-1} < v < +1500 \text{ km s}^{-1}$), I achieve good fits to the overall line profiles at these epochs.

4.2.2 The evolution of the maximum and minimum velocities

For a freely expanding medium, the velocity of any fractional radial element should not change with time. The maximum velocity of any line-emitting region is therefore expected to be constant. However, at the epochs I consider here, it appears that the maximum velocities of the H α line, as determined by the velocity at zero intensity on the blue side, generally increase over time (see Table 4.2). I attribute this to the start of the freeze-out phase in the outer regions of the ejecta, while the hydrogen neutral fraction is still increasing in the denser inner regions (Danziger et al. 1991b; Fransson & Kozma 1993).

Table 4.2. H α full-width half-maxima (FWHM) and the half-width zero intensities (HWZI) determined by the zero intensity velocity on the blue side of the line. The tabulated line widths have been corrected for the relevant instrumental resolution.

day	FWHM (\AA)	HWZI (\AA)
524	3200	3600
611	2700	3400
673	1600	3700
714	3100	4500
806	3200	5500
1054	2100	5600
1478	1400	6600
1862	1600	6800
2211	1400	6700
2875	2700	6700
3500	3500	7000
3604	2100	7000

The onset of a fixed ionization structure in the ejecta causes the rate of H α flux decline to slow. Since the outer, faster moving regions reach this state at earlier times than the inner, slower moving regions, the relative flux contribution of the outer regions is increased. At early epochs ($t < 900$ days) the flux contribution from hydrogen in the core dominates the overall H α flux, whereas at later epochs ($t > 900$ days) the flux from the envelope dominates (Fransson & Kozma 1993; Kozma & Fransson 1998a). This shift likely explains apparent broadening of the line with the higher velocity material becoming increasingly noticeable in the line profiles. This may also explain the increase in half-width zero intensity (HWZI) velocities at these epochs with the relative flux from the very densest regions dropping more rapidly relative to the outer line-emitting region. The full-width half maximum (FWHM) remains relatively steady (see Table 4.2). However, the FWHM values presented in Table 4.2 were difficult to determine accurately since the peak of the broad line profile is contaminated by narrow line emission from the ER.

4.3 Modelling SN 1987A

I have modelled the H α line of SN 1987A at days 714, 806, 1862, 2211, 2875, 3500 and 3604, and the [O I] $\lambda\lambda 6300, 6363$ \AA doublet at days 714, 806, 1054 and 1478. After day 3604 the H α profile begins to become dominated by emission from the reverse shock and the structure of the emitting region may no longer be approximated by a single shell model

Table 4.3. Observed luminosities of the H α line and estimated electron scattering optical depths from R_{in} to R_{out} for the radii detailed in Tables 4.4 to 4.5 based on an assumed gas temperature of 10,000 K.

day	H α		[O I]		
	L_{obs} (10^{37} erg s $^{-1}$)	L_{undep}/L_{obs}	L_{obs} (10^{37} erg s $^{-1}$)	L_{undep}/L_{obs}	τ_e (10^{-2})
714	1.36	1.65	0.313	3.57	1.44
806	0.57	1.77	0.0942	3.57	0.840
1054			0.0242	3.23	
1478			0.00185	2.70	
1862	0.0063	2.06			0.159
2211	0.0041	2.07			0.0378
2875	0.0019	2.84			0.0219
3500	0.00079	3.16			0.0125
3604	0.00098	3.27			0.0149

as I do here (Fransson et al. 2013). The [O I] $\lambda 6300, 6363$ Å doublet becomes too weak to model after day 1478 (see Figure 4.5). I continue to adopt a velocity profile $V(r) = \frac{V_{max}}{R_{max}} r$ and treat the variable parameters listed at the start of Section 3.2. Whilst the albedo and optical depth are not varied directly, they are altered by adjusting the dust mass, M_{dust} , and the grain radius, a , which together determine the albedo and optical depth via Mie theory and the optical properties of the dust.

In all models, the ejecta occupies a shell with inner radius R_{in} and outer radius R_{out} . Packets are emitted according to a smooth density profile assuming recombination or collisional excitation such that $i(r) \propto \rho(r)^2 \propto r^{-2\beta}$. Initially the dust is considered to have a smooth density distribution and is assumed to be coupled to the gas so as to follow the same radial profile. A clumped distribution of dust is considered later (see Section 4.3.2).

Assuming an electron temperature of 10,000 K, I estimated the total electron scattering optical depths between R_{in} and R_{out} based on the observed fluxes of the H α recombination line. A temperature of 10,000 K for the recombining material is likely too high at the epochs considered but I adopt it in order not to underestimate electron scattering optical depths. The values I calculate from the observed H α luminosities are listed in Table 4.3. Since the electron scattering optical depths at these epochs are negligibly small I therefore do not include electron scattering in the models.

There is rarely a unique set of parameters that provide the best fit to the data. However, the majority of the parameters of interest can be well constrained from my modelling

by considering different elements of the shape of the profile. In particular, by constructing fits to the data using minimum and maximum limits for the grain radius, credible lower and upper bounds on the dust mass formed within the ejecta may be derived. I present here fits to the data obtained using both small and large values of the grain radius a since it is the grain radius which has the most significant effect on the overall dust mass required to reproduce the line profile (see Section 3.2).

All of my models are of a dusty medium composed solely of amorphous carbon grains. I use the optical constants from the BE sample presented by Zubko et al. (1996). Although previous SED modelling of SN 1987A limited the fraction of silicates present in the dusty ejecta to a maximum of 15% (Ercolano et al. (2007), W15), the recent work of Dwek & Arendt (2015) has suggested that a large mass of mostly silicate dust may have formed at early epochs (~ 615 days). It is therefore useful to consider the effects on my models of using silicate dust. I discuss this in detail in Sections 4.3.7 and 4.3.8.

For each profile, the maximum velocity is initially identified from the data as the point where the emission vanishes on the blue side and is then varied throughout the modelling in order to produce the best fit. The equivalent point on the red side is indeterminate from observations due to the effects of dust scattering. I determine the approximate value of V_{min} by examining the width of the profile near its peak. Using the features and shapes presented in Figures 3.6 and 3.7 as a guide, I first examined the observed profile for any obvious points of inflection or abrupt changes in the steepness of the profile. If these were observed then they were compared to similar changes in theoretical profiles which allowed me to estimate the value of V_{min} . If none were observed, then a model setting V_{min} to be the velocity of the profile peak was considered. Where neither of these approaches yielded a good model (this was rare) I iterated over a range of values of V_{min} as with other variable parameters such as the dust mass. On the red side the theoretical minimum velocity often falls at a similar velocity to the narrow nebular [N II] 6583Å line so any dust-induced features near this wavelength that would allow a more accurate determination of V_{min} can be overwhelmed by the nebular line. Having determined the minimum and maximum velocities, the ratio of the inner and outer radii of the supernova ejecta can be determined since $R_{in}/R_{out} = V_{min}/V_{max}$. The outer radius is calculated from the epoch and the maximum velocity.

The only parameters that remain to be determined are the exponent of the density profile β , the mean grain radius and the total dust mass. The shape of the blue wing is

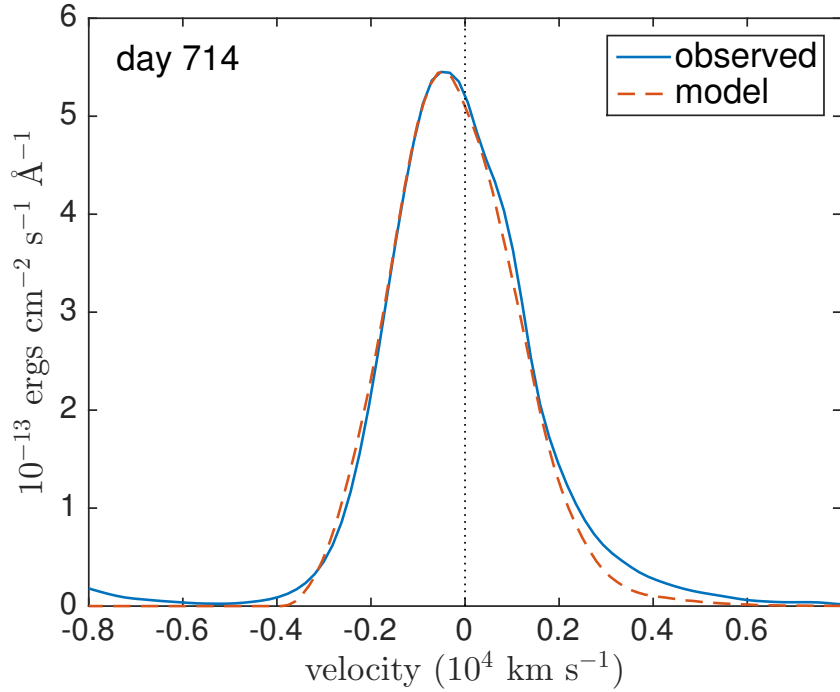


Figure 4.8. Amorphous carbon smooth dust fit to the day 714 H α line of SN 1987A using an MRN size distribution, illustrating the underestimation of the red scattering wing for small grain radii. Model parameters are the same as the smooth dust fit for day 714 (Table 4.4) except for the grain radius distribution and dust mass: $M_{dust} = 8.0 \times 10^{-6} M_{\odot}$, $a_{min} = 0.005 \mu\text{m}$, $a_{max} = 0.25 \mu\text{m}$ and $n(a) \propto a^{-3.5}$.

solely a product of the density profile and the dust mass; the height and shape of the red wing is a product of these and also of the scattering efficiency of the grains (the albedo ω); the extent and shape of the asymmetry in the flat-topped portion of the profile is a function of only the total dust optical depth determined by the dust mass and the grain radius. By iterating over these three parameters, an excellent fit to the data can usually be obtained.

Models are produced in the same manner for the [O I] $\lambda 6300, 6363 \text{ \AA}$ doublet as for the single H α line, with each component of the doublet being modelled independently and the resulting profiles added according to a specified ratio. Although the theoretical intrinsic flux ratio is 3.1 for optically thin emission (Storey & Zeippen 2000), the actual ratio between the two components can be affected by self-absorption (Li & McCray 1992) and I therefore left it as a free parameter. The deduced doublet ratios are listed in Tables 4.4, 4.5 and 4.6.

For all lines, though particularly at very late epochs, even small fluctuations in the

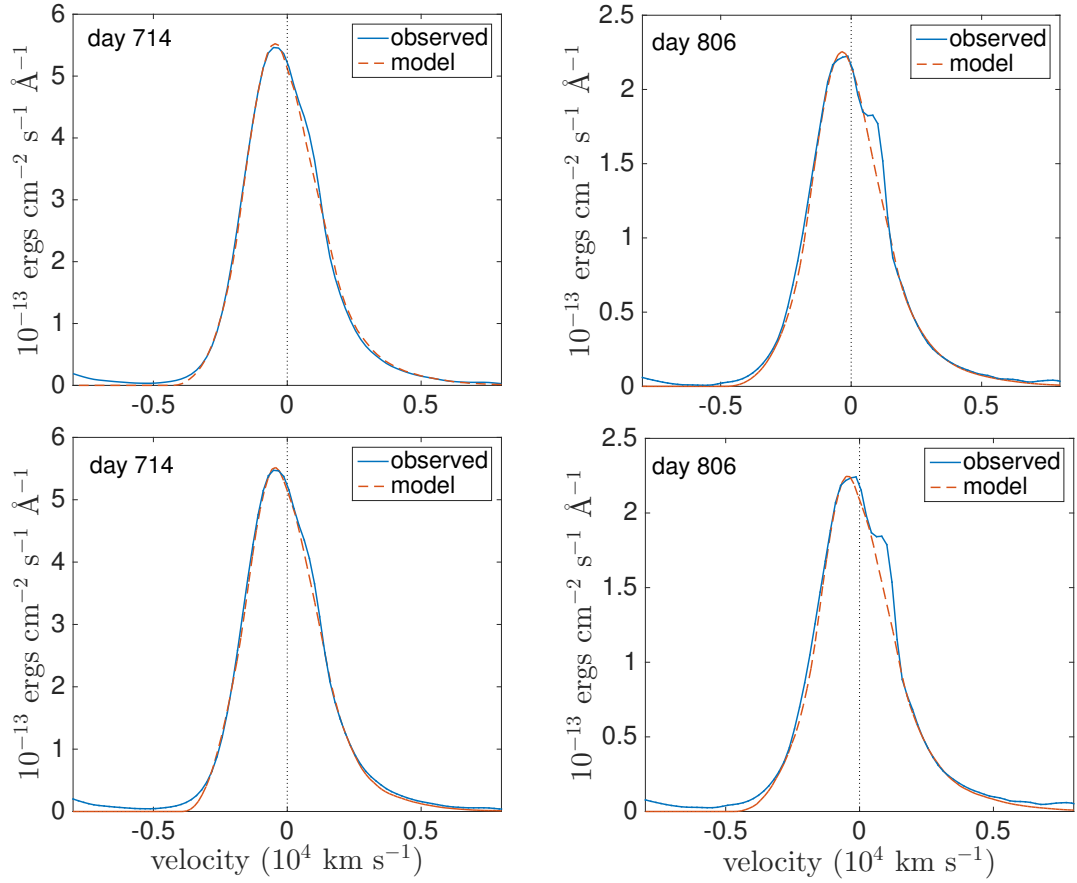


Figure 4.9. Best model fits to the SN 1987A H α line at day 714 and day 806 for the parameters detailed in Tables 4.4 and 4.5. The two fits on the top are smooth dust models using amorphous carbon grains of radius $a = 0.35 \mu\text{m}$ and the two fits on the bottom are clumped dust models using amorphous carbon grains of radius $a = 0.6 \mu\text{m}$.

adopted value of the continuum level can have a substantial effect on the fit to the resulting profile. Since it is not feasible to establish the level of the continuum so precisely, the value of the continuum has been left as a free parameter that may be adjusted (to within sensible margins) in order to allow for the widest possible dust mass range to be determined. I generally find it is necessary to assume a continuum level that is slightly lower where the dust mass is higher. The [O I] $\lambda\lambda 6300, 6363 \text{ \AA}$ doublets at days 1054 and 1478 are weak relative to the continuum and are also blended with the wings of other lines making it difficult to fit their wings accurately. I aim to fit the lines between approximately -3000 km s^{-1} and $+5000 \text{ km s}^{-1}$ but present a wider velocity range for context (for example see Figure 4.11).

Fits to the H α line profile at days 2211 and 3500 are omitted for the sake of space

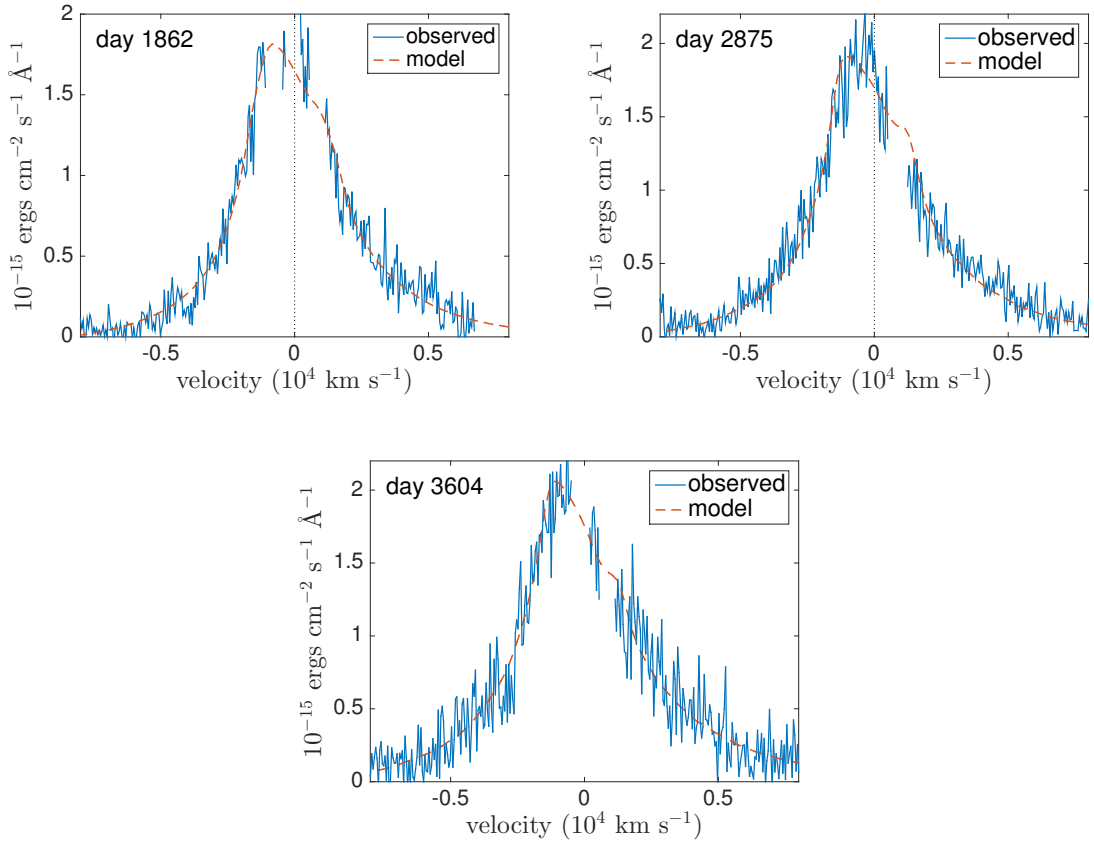


Figure 4.10. Best model fits to the SN 1987A H α line at days 1862, 2875 and 3604 for the parameters detailed in Tables 4.4. Smooth model fits with amorphous carbon grains of radius $a = 0.35 \mu\text{m}$ are presented.

but are very similar to those of days 1862 to 3604. All profiles have been smoothed to approximately the same resolution as the observed profiles using a moving-average procedure. Parameters for the models at all epochs including days 2211 and 3500 are detailed in Tables 4.4 to 4.6.

4.3.1 Smooth Density Models for SN 1987A

Even at the earliest epochs there is a substantial wing on the red side of the H α line profile that cannot be fitted by scattering from moving grains with a low albedo. The minimum required albedo is approximately $\omega \approx 0.5$ implying relatively large grain radii. As previously discussed, the larger the grain radius the larger the mass of dust required to reproduce the same optical depth. Figure 4.8 illustrates the fit for the day 714 H α profile for the case where a classic MRN (Mathis et al. 1977) grain radius distribution is adopted, with $a_{min} = 0.005 \mu\text{m}$, $a_{max} = 0.25 \mu\text{m}$ and $n(a) \propto a^{-3.5}$. It can be seen clearly

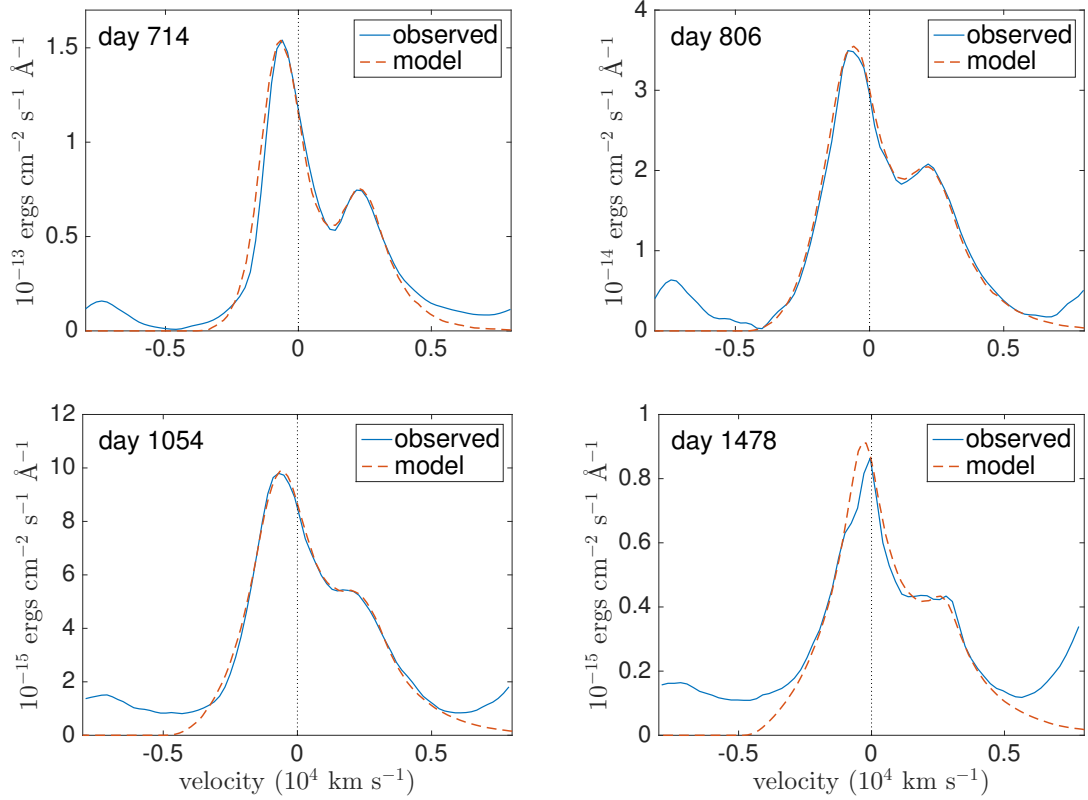


Figure 4.11. Best smooth dust fits to the SN 1987A [O I] $\lambda\lambda 6300, 6363$ Å doublet at days 714, 806, 1054 and 1478 for the parameters detailed in Tables 4.4. Smooth dust fits with amorphous carbon grains of radius $a = 0.35\mu\text{m}$ are presented.

that the extended red wing is significantly underestimated. Since the albedo of amorphous carbon grains varies significantly with grain radius (see Figure 3.9) I can establish a strong lower bound to the mean dust grain radius, which I estimate to be $a \geq 0.35\mu\text{m}$. This is the smallest grain radius that is still capable of reproducing the red scattering wing at all epochs and I therefore use this lower limit value throughout my smooth density modelling.

The inner and outer radii of the ejecta are calculated at each epoch from the maximum velocity used, the day number and the specified ratio R_{in}/R_{out} . The radii generated are consistent with those used in previous models of SN 1987A (Ercolano et al. (2007), W15) and the minimum velocities for both the [O I] and H α line emitting regions are relatively consistent with those obtained by Kozma & Fransson (1998b) who estimate that hydrogen extends into the core to a depth of $\lesssim 700\text{ km s}^{-1}$ and the oxygen reaches down to $\sim 400\text{ km s}^{-1}$. They are also consistent with predictions from 3D explosion models at the time of shock-breakout that predict the oxygen to reach to a depth of $\sim 200\text{ km s}^{-1}$ (Hammer et al. 2010; Wongwathanarat et al. 2015). Figures 4.9 to 4.11 show the best fits

Table 4.4. The parameters used for the best fitting smooth models of SN 1987A with amorphous carbon grains of radius $a = 0.35 \mu\text{m}$. Optical depths are given from R_{in} to R_{out} at $\lambda = 6563 \text{ \AA}$ for H α and $\lambda = 6300 \text{ \AA}$ for [O I]. Values of τ_V are very close to the quoted values of $\tau_{H\alpha}$.

	day	V_{max} (km s $^{-1}$)	V_{min} (km s $^{-1}$)	R_{in}/R_{out}	β	M_{dust} (M_\odot)	R_{out} (cm)	R_{in} (cm)	[O I] ratio	τ_λ
[O I]	714	3250	228	0.07	2.9	9.65×10^{-5}	2.00×10^{16}	1.40×10^{15}	2.6	3.60
[O I]	806	4000	240	0.06	2.4	1.50×10^{-4}	2.79×10^{16}	1.67×10^{15}	2.3	2.86
[O I]	1054	4300	215	0.05	2.1	2.35×10^{-4}	3.92×10^{16}	1.96×10^{15}	2.7	2.23
[O I]	1478	4500	180	0.04	1.7	2.95×10^{-4}	5.75×10^{16}	2.30×10^{15}	3.0	1.30
H α	714	3250	813	0.25	1.2	2.10×10^{-5}	2.00×10^{16}	5.01×10^{15}	0.61	
H α	806	4000	880	0.22	1.9	3.80×10^{-5}	2.79×10^{16}	6.13×10^{15}	0.59	
H α	1862	8500	1275	0.15	1.9	5.00×10^{-4}	1.37×10^{17}	2.05×10^{16}	0.35	
H α	2211	9000	1260	0.14	1.9	9.25×10^{-4}	1.72×10^{17}	2.41×10^{16}	0.42	
H α	2875	9500	1330	0.14	1.9	1.50×10^{-3}	2.36×10^{17}	3.30×10^{16}	0.36	
H α	3500	10000	1400	0.14	1.9	3.35×10^{-3}	3.02×10^{17}	4.23×10^{16}	0.49	
H α	3604	10250	1333	0.13	1.9	4.20×10^{-3}	3.19×10^{17}	4.15×10^{16}	0.55	

Table 4.5. The parameters used for the best fitting clumped models of SN 1987A with amorphous carbon grains of radius $a = 0.6 \mu\text{m}$. Optical depths are given from R_{in} to R_{out} at $\lambda = 6563 \text{ \AA}$ for H α and $\lambda = 6300 \text{ \AA}$ for [O I]. Values of τ_V are very close to the quoted values of $\tau_{H\alpha}$.

	day	V_{max} (km s $^{-1}$)	V_{min} (km s $^{-1}$)	R_{in}/R_{out}	β	M_{dust} (M_\odot)	R_{out} (cm)	R_{in} (cm)	[O I] ratio	τ_λ
[O I]	714	3250	228	0.07	2.7	2.00×10^{-4}	2.00×10^{16}	1.40×10^{15}	2.3	3.84
[O I]	806	4000	240	0.06	2.3	4.00×10^{-4}	2.79×10^{16}	1.67×10^{15}	2.0	4.02
[O I]	1054	4300	215	0.05	2.3	7.50×10^{-4}	3.92×10^{16}	1.96×10^{15}	2.3	3.85
[O I]	1478	4500	180	0.04	2.0	1.10×10^{-3}	5.75×10^{16}	2.30×10^{15}	2.8	2.65
H α	714	3250	813	0.25	1.4	5.50×10^{-5}	2.00×10^{16}	5.01×10^{15}	0.87	
H α	806	4000	880	0.22	1.8	9.00×10^{-5}	2.79×10^{16}	6.13×10^{15}	0.76	
H α	1862	8500	1190	0.14	1.9	1.20×10^{-3}	1.37×10^{17}	1.91×10^{16}	0.46	
H α	2211	9000	1260	0.14	1.9	3.00×10^{-3}	1.72×10^{17}	2.41×10^{16}	0.73	
H α	2875	9500	1140	0.12	2	8.00×10^{-3}	2.36×10^{17}	2.83×10^{16}	1.05	
H α	3500	10000	1200	0.12	2	1.35×10^{-2}	3.02×10^{17}	3.63×10^{16}	1.08	
H α	3604	10250	1230	0.12	2	1.70×10^{-2}	3.19×10^{17}	3.83×10^{16}	1.22	

Table 4.6. The parameters used for the best fitting clumped models of SN 1987A with amorphous carbon grains of radius $a = 3.5 \mu\text{m}$. Optical depths are given from R_{in} to R_{out} at $\lambda = 6563 \text{ \AA}$ for H α and $\lambda = 6300 \text{ \AA}$ for [O I]. Values of τ_V are very close to the quoted values of $\tau_{H\alpha}$.

	day	V_{max} (km s $^{-1}$)	V_{min} (km s $^{-1}$)	R_{in}/R_{out}	β	M_{dust} (M_\odot)	R_{out} (cm)	R_{in} (cm)	[O I] ratio	τ_λ
[O I]	714	3250	228	0.07	2.9	1.50×10^{-3}	2.00×10^{16}	1.40×10^{15}	2.3	4.20
[O I]	806	4000	240	0.06	2.3	2.70×10^{-3}	2.79×10^{16}	1.67×10^{15}	2.1	3.95
[O I]	1054	4300	215	0.05	2.3	5.50×10^{-3}	3.92×10^{16}	1.96×10^{15}	2.5	4.12
[O I]	1478	4500	180	0.04	1.9	8.00×10^{-3}	5.75×10^{16}	2.30×10^{15}	2.8	2.81
H α	1862	8500	1190	0.14	1.9	1.00×10^{-2}	1.37×10^{17}	1.91×10^{16}	0.55	
H α	2211	9000	1260	0.14	1.9	2.40×10^{-2}	1.72×10^{17}	2.41×10^{16}	0.85	
H α	2875	9500	1140	0.12	2	6.00×10^{-2}	2.36×10^{17}	2.83×10^{16}	1.15	
H α	3500	10000	1200	0.12	2	1.15×10^{-1}	3.02×10^{17}	3.63×10^{16}	1.34	
H α	3604	10250	1230	0.12	2	1.25×10^{-1}	3.19×10^{17}	3.83×10^{16}	1.31	

to the data for days 714 to 3604 whilst Table 4.4 details the parameters used.

It can be seen from Tables 4.4 to 4.6 that, in order to reproduce the blueshifts seen in the [O I] $\lambda 6300, 6363$ Å doublet, considerably larger dust masses are required than to fit the H α line at the same epoch. Although the same maximum velocities and therefore outer radii are used in my [O I] and H α models, the inner radii for the [O I] models are significantly smaller and the density distribution much steeper. This implies that [O I] is concentrated towards the centre of the ejecta whereas H α is more diffuse. This is broadly in agreement with 3D explosion dynamics models that suggest that a few hours after the explosion the heavier elements will, in comparison to hydrogen, be located more centrally in the ejecta with “bullets” of heavier material reaching the outer edges (Hammer et al. 2010). If dust is forming in the inner regions of the ejecta then the majority of the [O I] emission must travel through the newly formed dust whereas the more diffuse H α emission has a greater chance of escaping unaffected. This may explain the difference between the dust masses needed for the [O I] and H α models.

4.3.2 Clumped Dust Models for SN 1987A

A number of investigators have presented arguments for the material in the ejecta of SN 1987A being clumped (Lucy et al. 1991; Li & McCray 1992; Kozma & Fransson 1998b) and so I consider clumped models for the ejecta dust to be more realistic than smoothly distributed dust models. It has been shown through the modelling of optical-IR SEDs that when dust is assumed to have a clumped distribution then the derived dust masses can be significantly larger than for the case of dust that is distributed smoothly between the inner and outer radii (e.g. Ercolano et al. (2007); Owen & Barlow (2015)). I present two sets of fits to the line profile based on the clumped dust modelling of W15, one set with a minimum grain radius and one set with a maximum grain radius. Each fit is based on the best fitting smooth model such that the photon packets are emitted assuming a smooth radial density profile. However, the dust is no longer coupled to the gas but instead is located entirely in clumps of size $R_{out}/25$. The clumps are distributed stochastically between R_{in} and R_{out} with the probability of a given grid cell being a clump proportional to $r^{-\beta}$ where $i(r) \propto r^{-2\beta}$. The number of clumps used is determined by the clump filling factor f which is kept constant at $f = 0.1$. All properties are fixed from the smooth models with the exception of the grain radius, density profile exponent (β) and the total dust mass.

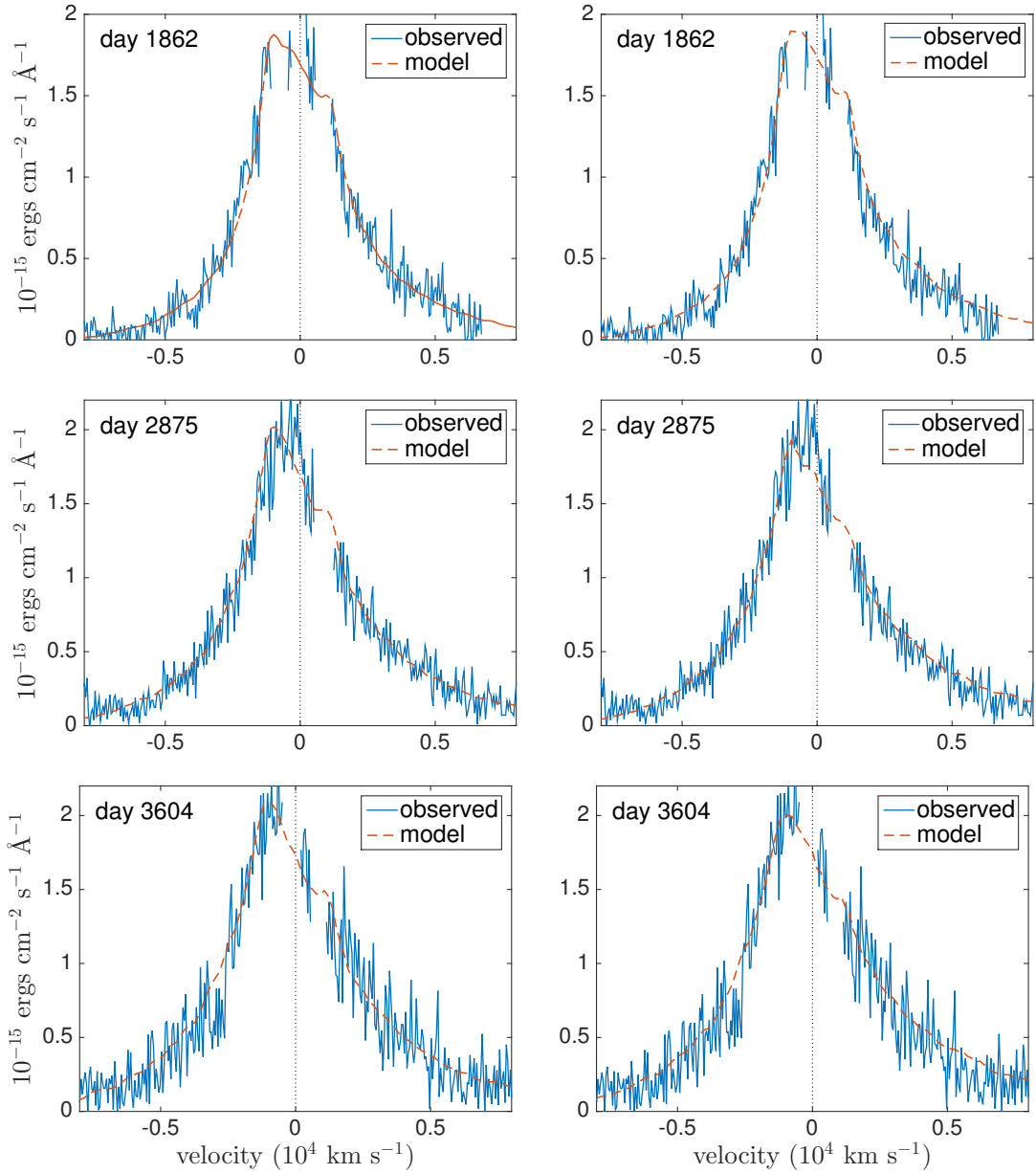


Figure 4.12. Best model fits to the SN 1987A H α line at days 1862, 2875 and 3604 for the parameters detailed in Tables 4.5 and 4.6. On the left are clumped model fits with amorphous carbon grains of radius $a = 0.6 \mu\text{m}$ and on the right are clumped model fits with amorphous carbon grains of radius $a = 3.5 \mu\text{m}$.

Models were again constructed using the smallest possible grain radius ($a=0.6\text{ }\mu\text{m}$ in the clumped case) in order to derive minimum dust masses for clumped distributions. By considering the extent of the red scattering wing, upper limits to the grain radius were also derived with the purpose of limiting the maximum dust mass at each epoch. By steadily reducing the grain radius from an initial value of $5\text{ }\mu\text{m}$ (motivated by the maximum possible grain radius derived by W15 for their day 8515 model), I produced a set of models with a maximum grain radius of $a = 3.5\text{ }\mu\text{m}$.

The increase in grain radius from the smooth case to the clumped case is necessary in order to have a slightly larger albedo. Grains of radius $a = 0.35\text{ }\mu\text{m}$ do not reproduce the red side of the profiles well for a clumped medium. This is because when the dust is located in clumps the radiation is subject to less scattering as well as to less absorption. The reduction in scattering appears not to be compensated for by the increased dust mass and a larger grain radius is therefore required, particularly at day 714.

For all but the $\text{H}\alpha$ line at days 714 and 806 a similar fit could be obtained with either a grain radius of $a = 0.6\text{ }\mu\text{m}$ or $a = 3.5\text{ }\mu\text{m}$ (see Figures 4.9 and 4.12). However, for $\text{H}\alpha$ at days 714 and 806 even a small change to the grain radius from $0.6\text{ }\mu\text{m}$ resulted in a significantly poorer fit, either over- or under-estimating the red wing. I therefore conclude that the dust mass estimates produced for the $\text{H}\alpha$ lines at days 714 and 806 for a grain radius of $a = 0.6\text{ }\mu\text{m}$ are the best $\text{H}\alpha$ -based estimates of the dust mass at this epoch.

In my subsequent analyses, I adopt the values derived from my clumped models. Details of the parameters used are presented in Tables 4.5 and 4.6 and the fits are presented in Figures 4.9 and 4.12.

4.3.3 Goodness of fit

I detailed at the start of Section 4.3 the process by which parameters were constrained in order to obtain good fits to the data. These fits were judged both by eye and by minimising the mean square error between the model and the observed data for each line profile. The sensitivity of the fits to various parameters may be of interest and so, in Tables 4.7 and 4.8, I detail the mean square error (MSE) for the $\text{H}\alpha$ profile at days 714 and 2875 for a range of dust masses and density profile exponents. All other parameters were kept fixed at their best-fitting values for the clumped models of $\text{H}\alpha$ with a grain radius $a = 0.6\mu\text{m}$ as in Table 4.5. The line profiles for these models are presented in Figures 4.14 to 4.17.

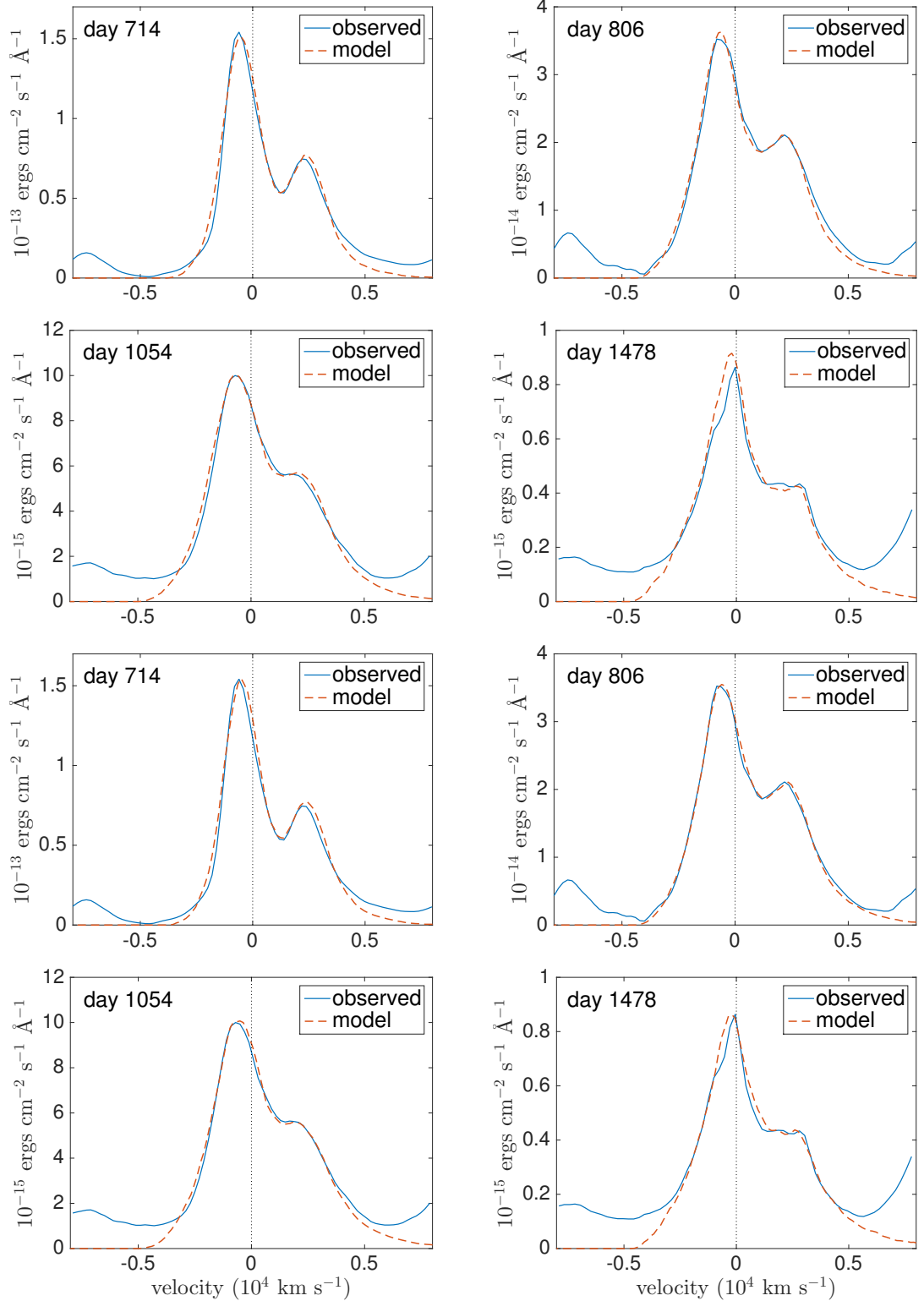


Figure 4.13. Best clumped model fits to the SN 1987A [O I] $\lambda 6300, 6363 \text{ \AA}$ doublet at days 714, 806, 1054 and 1478 for the parameters detailed in Tables 4.5 and 4.6. On the left are clumped dust fits with amorphous carbon grains of radius $a = 0.6 \mu\text{m}$ and on the right are clumped dust fits with amorphous carbon grains of radius $a = 3.5 \mu\text{m}$.

Table 4.7. Mean square errors illustrating the variation in goodness of fit for the H α line profile for a range of dust masses with other parameters fixed at their best-fitting values for the clumped model with $a = 0.6\mu\text{m}$ as detailed in Table 4.5. The MSE is calculated between -5000 km s^{-1} and $+7000 \text{ km s}^{-1}$ for the day 714 H α profile and between -8000 km s^{-1} and $+8000 \text{ km s}^{-1}$ for the day 2875 H α profile. A factor of zero represents the dust-free model. The best-fitting model is italicised.

	<i>multiple of best-fit mass</i>				
	0	0.1	0.5	1.0	2.0
Day 714 MSE ($10^{-13} \text{ ergs cm}^{-2} \text{ s}^{-1}$)	0.167	0.133	0.043	<i>0.005</i>	0.115
Day 2875 MSE ($10^{-15} \text{ ergs cm}^{-2} \text{ s}^{-1}$)	0.0791	0.0604	0.0258	<i>0.0182</i>	0.0563

Table 4.8. Mean square errors illustrating the variation in goodness of fit for the H α line profile for a range of density profiles with other parameters fixed at their best-fitting values for the clumped model with $a = 0.6\mu\text{m}$ as detailed in Table 4.5. The MSE is calculated between -5000 km s^{-1} and $+7000 \text{ km s}^{-1}$ for the day 714 H α profile and between -8000 km s^{-1} and $+8000 \text{ km s}^{-1}$ for the day 2875 H α profile. The best-fitting model is italicised.

	<i>density profile exponent (β)</i>				
	1.0	1.2	1.4	1.6	1.8
Day 714 MSE ($10^{-13} \text{ ergs cm}^{-2} \text{ s}^{-1}$)	0.0328	0.0117	<i>0.005</i>	0.0184	0.0410
Day 2875 MSE ($10^{-15} \text{ ergs cm}^{-2} \text{ s}^{-1}$)	0.0282	0.0205	<i>0.0182</i>	0.0193	0.0255

The MSE is calculated as

$$\frac{1}{N} \sum_i (f_{obs,i} - f_{mod,i})^2 \quad (4.1)$$

where N is the number of data points, $f_{obs,i}$ is the observed flux at the i^{th} data point and $f_{mod,i}$ is the modelled flux at the i^{th} data point. The MSEs were calculated between -5000 km s^{-1} and $+7000 \text{ km s}^{-1}$ for the day 714 H α profile and between -8000 km s^{-1} and $+8000 \text{ km s}^{-1}$ for the day 2875 H α profile. Note that the MSEs should only be compared between models for a given observed line profile and not between different line profiles since each observation is associated with a different inherent error.

For day 714, I find that increasing or decreasing the total dust mass by a factor of two with all other parameters fixed causes a substantial increase in the mean square error (by factors of 23 and 8.6 respectively) effectively ruling out these values. For day 2875 a similar variation is seen but with the MSE varying by factors of 1.4 and 3.0 for each case. The narrower range of MSEs at day 2875 compared to day 714 is due to a noisier profile which results in a greater allowed range of good fits. The sensitivity of the goodness of fit to the dust mass and density profile is similar for the other modelled epochs.

4.3.4 The effects of clumping

As in the case of SED radiative transfer models, the dust masses required to reproduce the observations in the clumped scenario are considerably higher than for the smooth scenario. The dust masses differ between my smooth models for $a = 0.35 \mu\text{m}$ and clumped models for $a = 0.6 \mu\text{m}$ by a factor of approximately 3. The dust mass estimates are even larger when comparing clumped $a = 0.6 \mu\text{m}$ models to clumped $a = 3.5 \mu\text{m}$ models at later epochs. This does not take into account the increase in grain radius between the two cases however. This increase accounts for a reasonable fraction of this difference. I estimate the effects of clumping alone to increase the required dust mass by a factor of approximately 1.5-2.0 from the smooth case.

4.3.5 More complex models

Where blue-shifted lines are observed in the spectra of CCSNe it is often the case that the Balmer lines of HI are less affected than the [O I] lines (Milisavljevic et al. 2012).

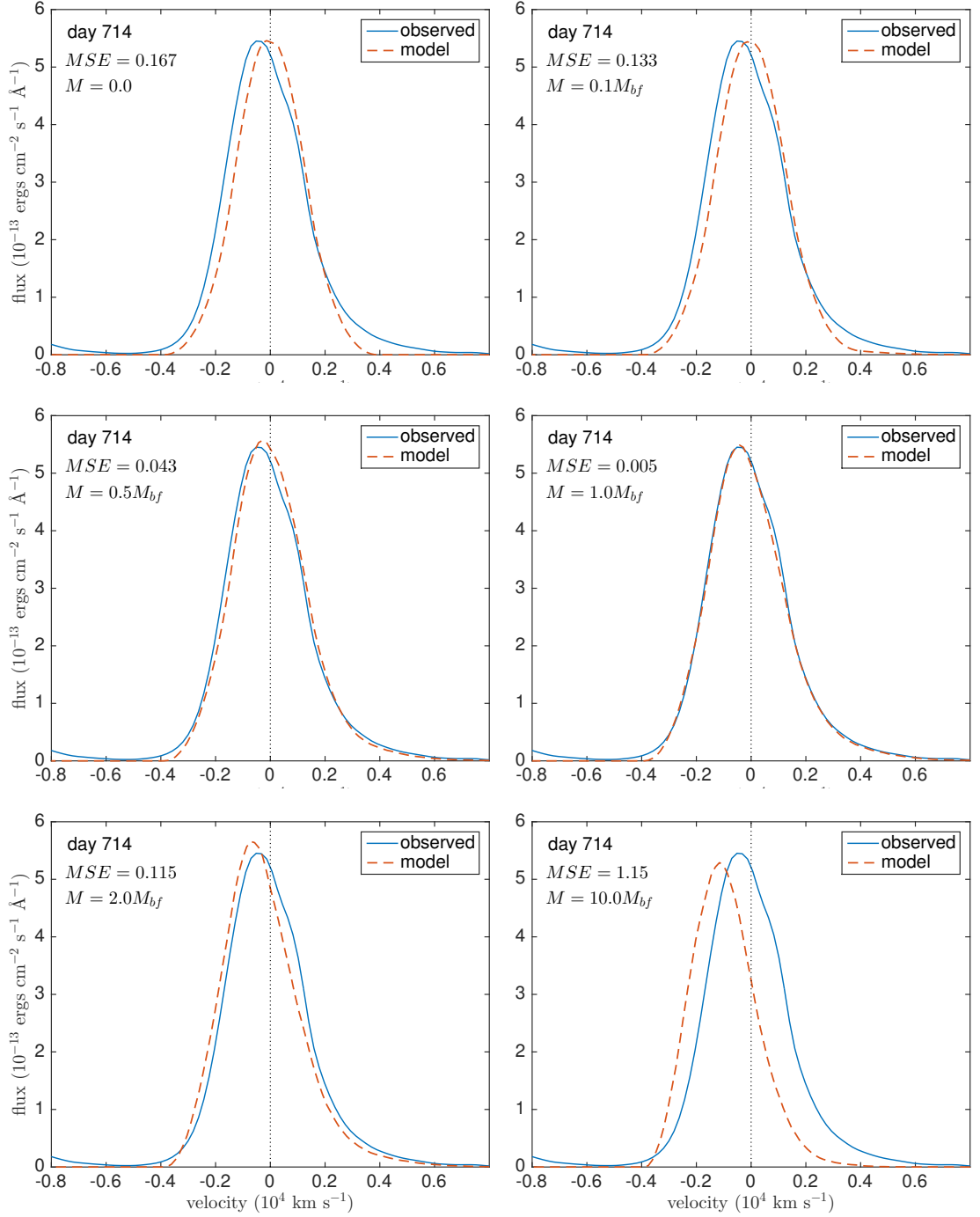


Figure 4.14. Fits to the H α line profile for day 714 for a variety of dust masses. All other parameters are given as per Table 4.5. Dust masses are given as a multiple of the best fitting dust mass (M_{bf}) and the mean squared error is presented for each plot.

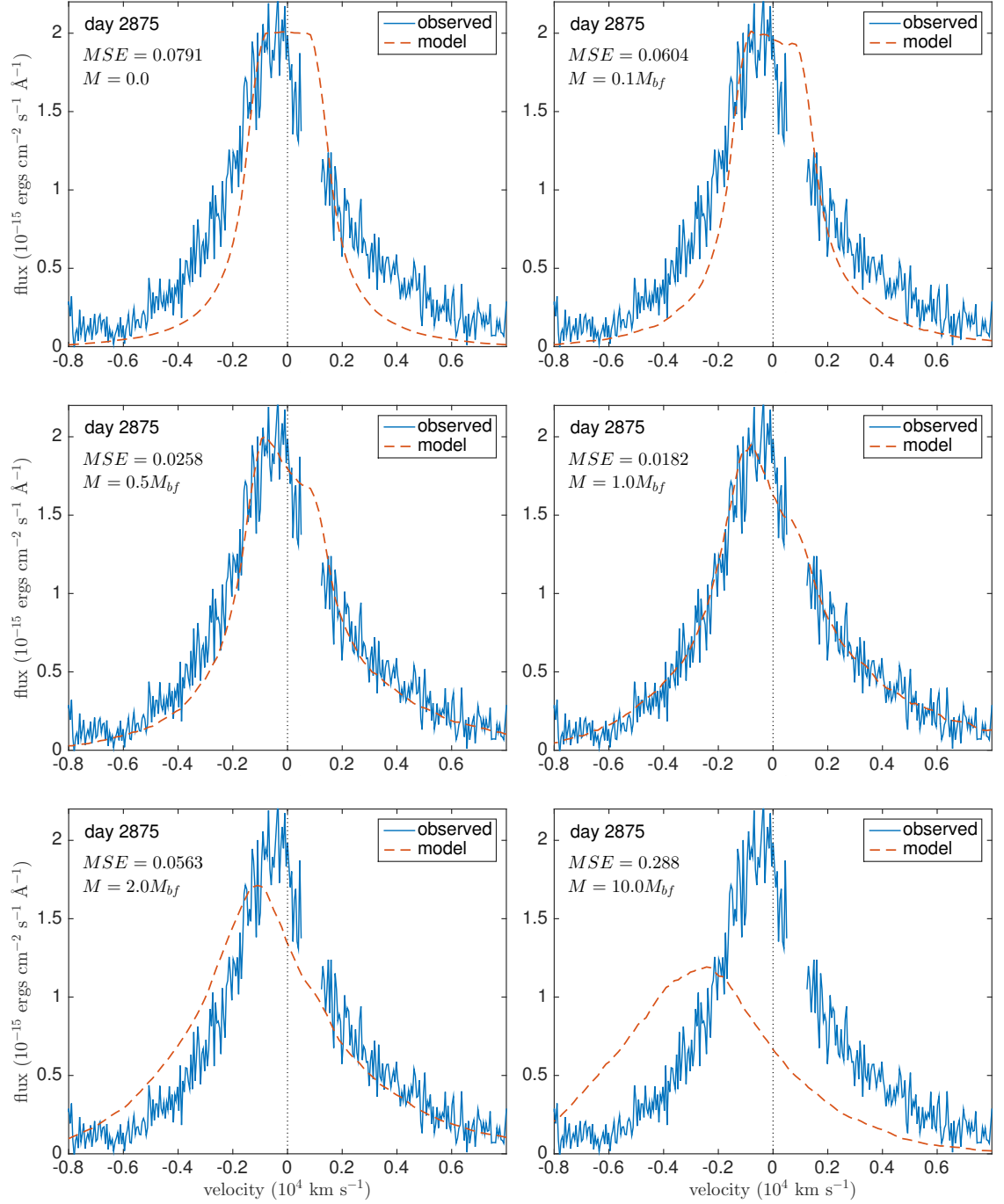


Figure 4.15. Fits to the H α line profile for day 2875 for a variety of dust masses. All other parameters are given as per Table 4.5. Dust masses are given as a multiple of the best fitting dust mass (M_{bf}) and the mean squared error is presented for each plot.

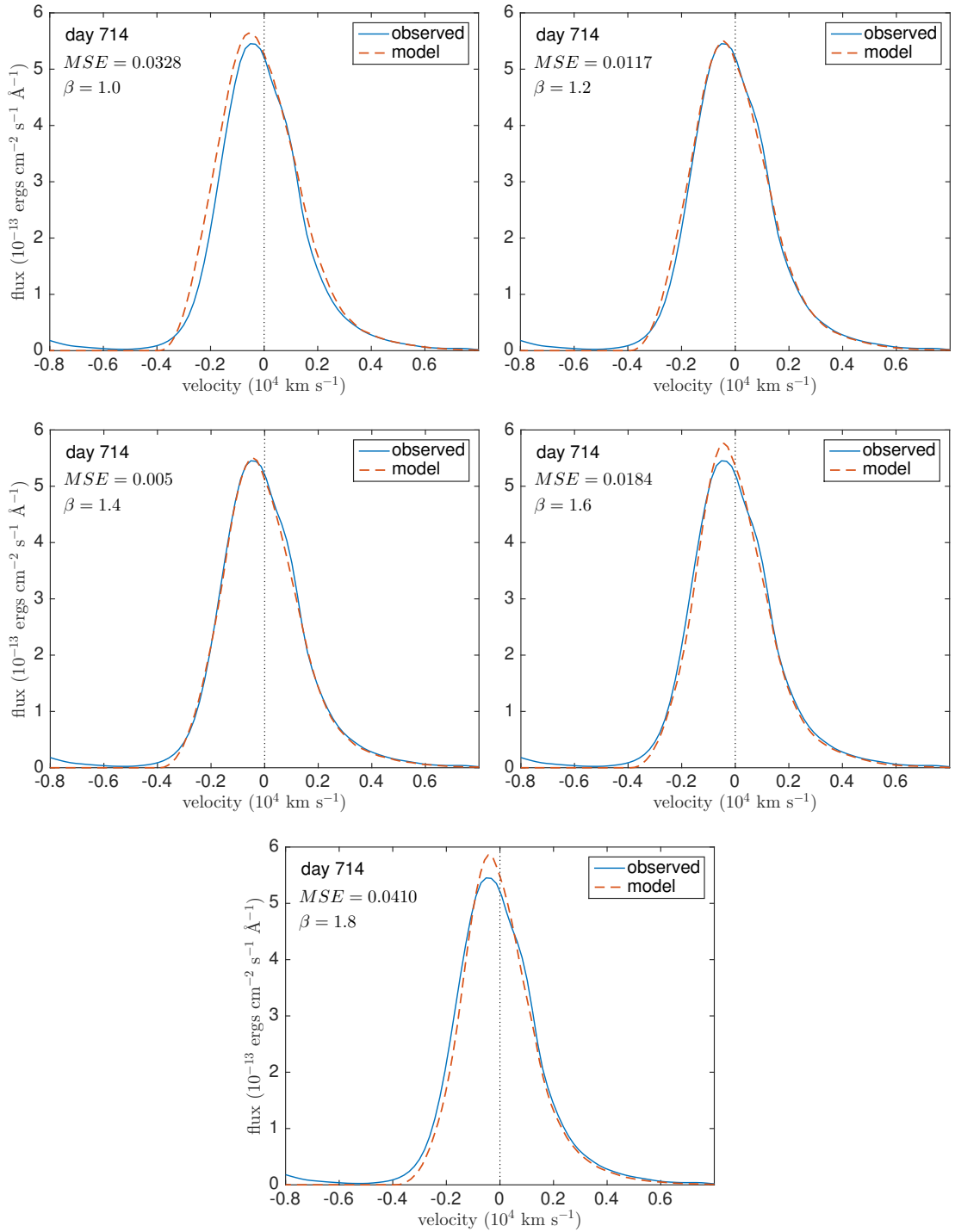


Figure 4.16. Fits to the H α line profile for day 714 for a variety of density distributions. All other parameters are given as per Table 4.5. The mean squared error is presented for each plot.

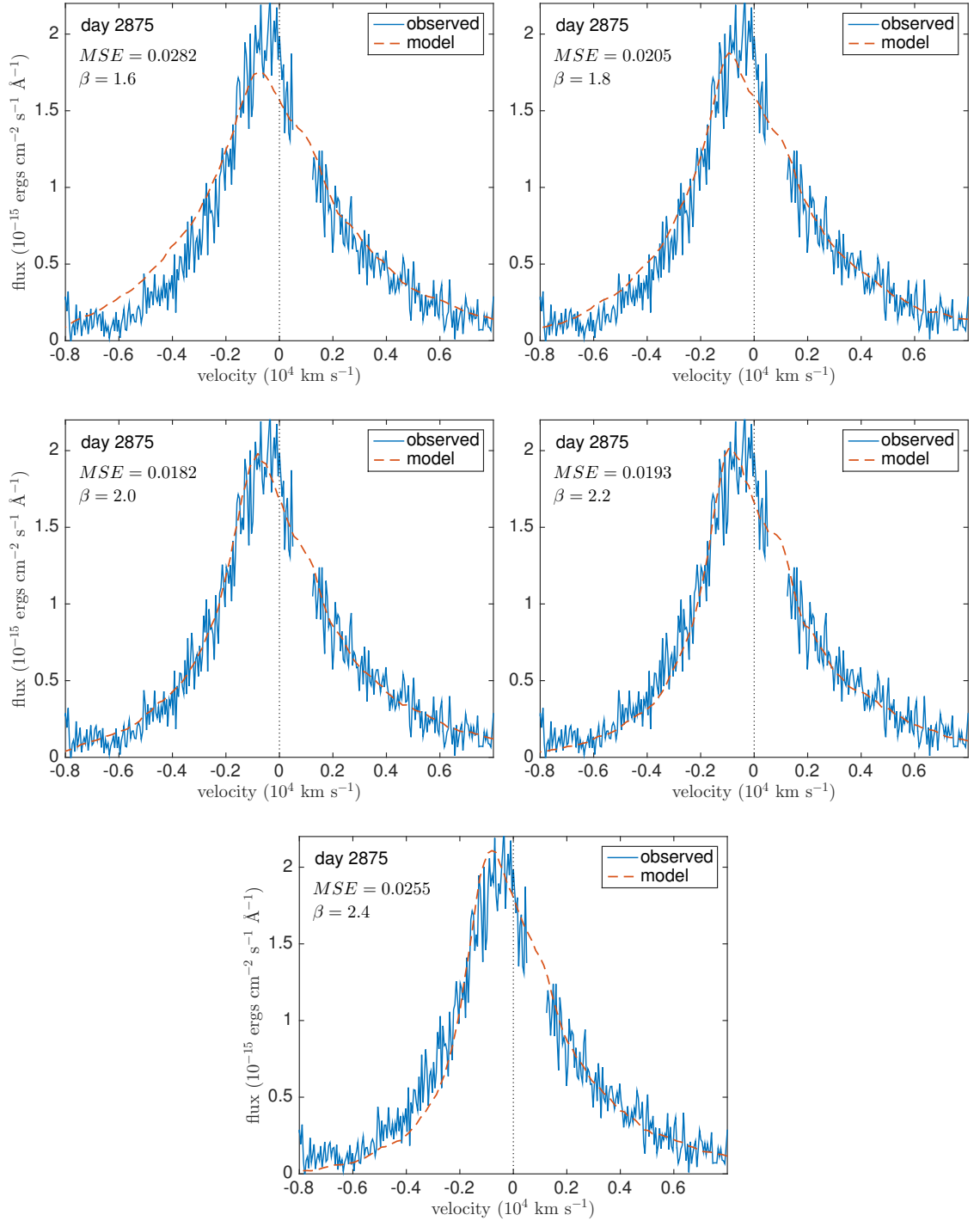


Figure 4.17. Fits to the H α line profile for day 2875 for a variety of density distributions. All other parameters are given as per Table 4.5. The mean squared error is presented for each plot.

This may be due to a difference in the location or distribution of the emitting elements; if the neutral hydrogen was diffusely distributed throughout the envelope but the oxygen was co-located with the dust in the core and in clumps then this could result in [O I] emission undergoing greater attenuation than H α . This geometry would be in line with previous models of SN 1987A that suggested that the dust-forming regions are likely to include those which are oxygen-rich (Kozma & Fransson 1998a). Clearly, any model of dust formation in the ejecta of a CCSN must consistently reproduce all of the line profiles at a given epoch. The models presented in this paper thus far have coupled the gas and dust distributions for a fixed clump volume filling factor and clump size. The H α and [O I] models therefore require different dust masses with the [O I] models usually requiring a dust mass ~ 4 times larger than the H α models.

I now present a model that reconciles this difference by additionally varying the clump filling factor, clump size and emissivity distribution. I assume that neutral hydrogen is likely diffuse throughout the ejecta and so maintains a smoothly distributed power-law emissivity distribution between R_{in} and R_{out} for H α . However, I now assume that dust mostly forms in dense regions of high metallicity and so restrict the [O I] $\lambda 6300, 6363$ Å emission to originate entirely from the dusty clumps. As previously discussed, the greater the covering factor of the dust the greater the albedo required in order to reproduce the H α red scattering wing. In order to obtain both the strong blue-shifting of the [O I] line and the extended red scattering wing observed in H α a small number of dense clumps were required along with a small mass of diffusely distributed highly scattering dust in the inter-clump medium.

In order to fit both line profiles simultaneously I required a very high albedo ($\omega > 0.8$) that demanded the inclusion of some fraction of silicate dust. Amorphous carbon grains alone are incapable of producing this level of scattering for any grain radius. I adopted a grain radius of $a = 0.6\mu\text{m}$, the same as that used in my initial clumped models and I varied the relative proportions of amorphous carbon and MgSiO₃ in order to achieve the necessary albedo. The adopted grain densities were $\rho_c = 1.85 \text{ g cm}^{-3}$ for amorphous carbon grains and $\rho_s = 2.71 \text{ g cm}^{-3}$ for MgSiO₃. The resulting dust model for day 714 used 75% MgSiO₃ and 25% amorphous carbon by cross-sectional area with a volume filing factor $f_V = 0.1$ and a clump size $R_{out}/5$. 90% of the dust mass was located in clumps with the remaining 10% distributed smoothly between R_{in} and R_{out} according to a power law $\rho \propto r$. Clumps were distributed stochastically with probability $\propto r^{-8}$ compared to $r^{-2.7}$

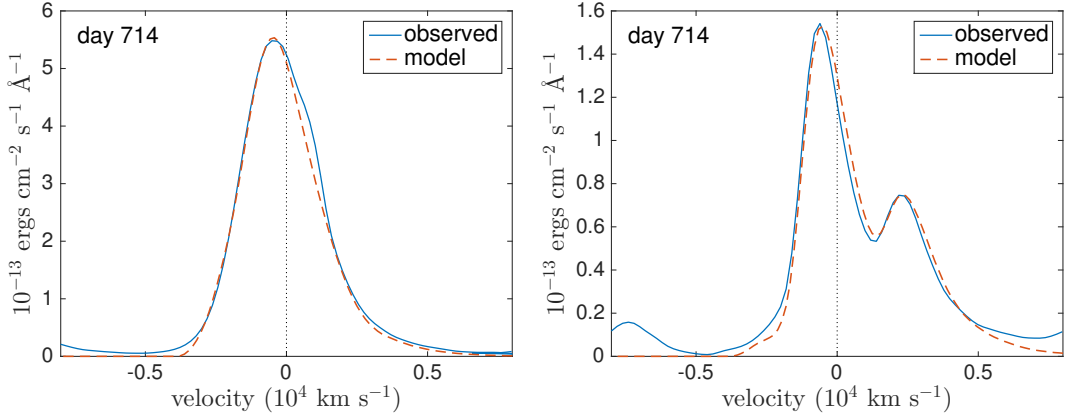


Figure 4.18. Fits to the H α and [O I] $\lambda\lambda 6300,6363$ Å lines at day 714 using the more complex dust model described in Section 4.3.5 with a dust mass of $2.3 \times 10^{-4} M_{\odot}$.

in my standard models discussed earlier. Equal numbers of [O I] packets were emitted from each clump. The increased steepness of the density profile is required to compensate for the clumped packet emission relative to the previous smooth distribution. Since the clumps are distributed stochastically according to the density profile, less flux is emitted from the central regions in a clumped emission model than in a smooth distribution model (since there are gaps between the clumps). In order to obtain a sufficiently steeply rising line profile, the density profile must therefore be steepened in clumped emission models. The adopted value of β does not significantly affect the best-fitting values of the other parameters of interest however. H α was distributed smoothly according to a density power law $\rho(r) \propto r^{-1.3}$. R_{out} was the same for all components (i.e. clumped dust, diffuse dust, [O I] emission and H α emission) and was calculated using a maximum velocity of 3250 km s $^{-1}$. The inner radius was $R_{in} = 0.07R_{out}$ for all components except the smooth H α emission which was emitted between $R_{in} = 0.25R_{out}$ and R_{out} .

The total dust mass used was $M_{dust} = 2.3 \times 10^{-4} M_{\odot}$. This dust mass is very similar to that derived from my original clumped models of [O I] using amorphous carbon grains of radius $a = 0.6 \mu\text{m}$. The slight increase over my amorphous carbon dust mass of $1.5 \times 10^{-4} M_{\odot}$ is largely due to the higher grain density of MgSiO₃. At this grain radius amorphous carbon and MgSiO₃ have similar extinction efficiencies and so the change in species and geometry does not substantially alter the dust mass. I therefore adopt the [O I] dust masses in my further analyses and consider the differences in my derived dust masses between H α and [O I] to be the result of the clumped emission of [O I].

Fits to both the [O I] λ 6300,6363 Å and H α lines for day 714 using these parameters are presented in Figure 4.18.

4.3.6 The effect of a grain radius distribution

All of the models heretofore have been based on a single grain radius. As previously discussed in Chapter 3, it is important to consider the possible effects of a dust grain radius distribution. This is more likely to be the case in reality and potentially has a significant effect on the derived dust mass.

As discussed in Section 4.3.1, for a classical MRN power law ($n(a) \propto a^{-3.5}$) with a wide grain radius range ($a_{min} = 0.001 \mu\text{m}$ to $a_{max} = 4.0 \mu\text{m}$) the derived albedo is much too small to reproduce the required wing seen at early epochs. I therefore adopt an approach whereby, for a number of grain radius ranges, I adjust the exponent of the distribution until the overall albedo is the same as that seen for the best fitting single grain radius for the clumped distributions. Using Equation 3.20 from Chapter 3, I calculate the required dust masses for the clumped H α model on day 714 for a selection of distributions with varying a_{min} . These are presented in Table 4.9.

It can be seen that in all cases, a larger dust mass is required for grain radius distributions in order to reproduce the same profile as a single grain radius. The conversion factors presented in the table are valid for any model with grain radius $a = 0.6 \mu\text{m}$ and may therefore also be applied to the models for day 806. I repeated the process for $a = 3.5 \mu\text{m}$ but found that, in order to reproduce the required albedo, the distribution had to be heavily weighted towards the larger grains and that the value of a_{min} had no effect on the required dust mass. Increasing the value of a_{min} to larger values ($> 2 \mu\text{m}$) does not have a significant effect either. This is because both extinction efficiency and albedo tend to a constant value with increasing grain radius and the adoption of different grain radius ranges and distributions above a certain threshold results in only insignificant variations in these quantities.

I conclude that if a distribution of grain radii is indeed present, the deduced single size dust masses are likely to under-estimate the true mass of newly formed dust.

4.3.7 The effect of different grain species

In my analyses so far I have mostly focussed on amorphous carbon as the species of interest. This was motivated by previously published early epoch optical and IR SED

Table 4.9. Dust masses for day 714 clumped models of the H α line using different grain radius distributions and 100% amorphous carbon. The final column shows the factor of increase over the dust mass for the single size model ($M = 7 \times 10^{-5} M_{\odot}$ with $a = 0.6 \mu\text{m}$) and p is the exponent of the grain radius distribution $n(a) \propto a^{-p}$.

a_{min} (μm)	a_{max} (μm)	p	M (M_{\odot})	$M/M_{0.6}$
0.001	4.0	2.45	1.93×10^{-4}	2.76
0.01	4.0	2.45	1.93×10^{-4}	2.76
0.05	4.0	2.52	1.84×10^{-4}	2.62
0.1	4.0	2.72	1.61×10^{-4}	2.3
0.5	4.0	8.20	7.23×10^{-5}	1.03

analyses that found that the silicate mass fraction must be limited to $\leq 15\%$ (Ercolano et al. (2007), W15). The recent suggestion by Dwek & Arendt (2015) that large masses of the glassy silicate MgSiO₃ may have formed at early epochs is discussed further in the next subsection. As previously discussed in Chapter 3, the parameters that affect the quantity of dust required by my models are the mean albedo and optical depth of the dust and there could therefore be multiple combinations of grain species and sizes that result in a good fit to the data.

In Chapter 3, I evaluated the required change in dust mass when a medium of 100% silicates was used instead of amorphous carbon (see Equation 3.21).

Because of the nature of the variation of albedo with grain radius for the Draine & Lee (1984) astronomical silicate (see Figure 3.9), there is often more than one silicate grain radius that will give rise to the same albedo at a given wavelength. Some of the possibilities and the resulting mass conversion factors between media composed of 100% Zubko BE amorphous carbon and 100% Draine & Lee silicates derived using Equation 3.21 in Chapter 3 are given in Table 4.10. For my best fitting amorphous carbon models with $a = 0.6 \mu\text{m}$ (the first two entries in Table 4.10), using any fraction of silicates with either $a = 0.6 \mu\text{m}$ or $a = 3.5 \mu\text{m}$ would increase the dust mass. However, for the case of an amorphous carbon grain radius of $a = 3.5 \mu\text{m}$ (the last three entries), using silicate dust would reduce the dust mass by a factor of about two relative to my amorphous carbon values.

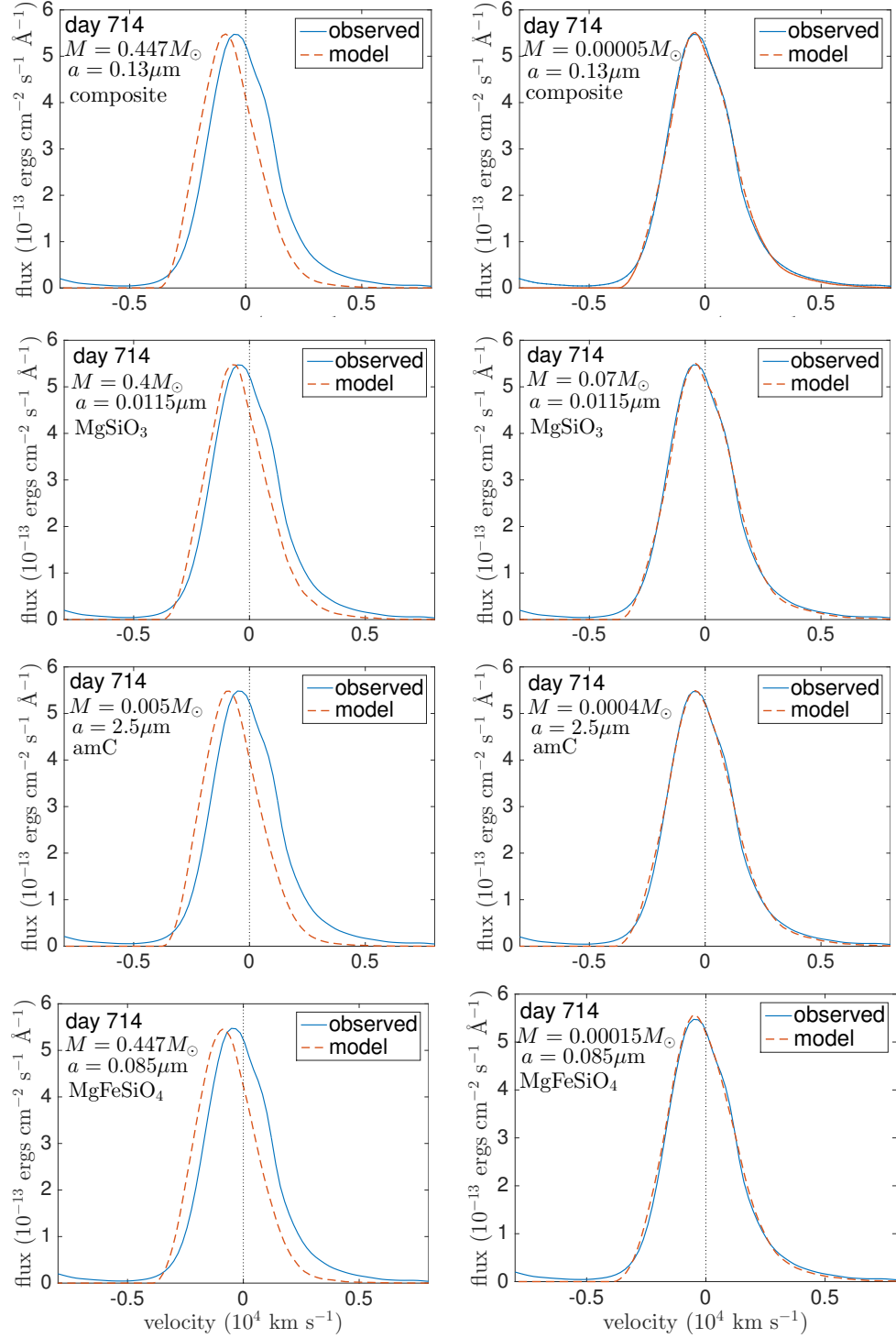


Figure 4.19. H α models using different grain species and dust masses. Models for the dust masses presented by Dwek & Arendt (2015) are on the top and models using my minimum required dust masses are on the bottom. From left to right the dust species are composite grains (82% MgSiO₃ and 18% amorphous carbon by volume), pure MgSiO₃, pure amorphous carbon and pure MgFeSiO₄. A density distribution with $\beta = 2.3$ was adopted with a filling factor $f = 0.09$ and an effective clump radius $R_{\text{eff}}/R_{\text{out}} = 0.044$. All other parameters are the same as in Table 4.5.

Table 4.10. Dust mass conversion factors for single size models using grains of 100% Zubko BE amorphous carbon or 100% Draine & Lee silicate at $\lambda \sim 656$ nm. f is the factor by which the dust mass changes on going from amorphous carbon to silicates.

carbon			silicates				
a (μm)	ω	Q_{ext}	a (μm)	ω	Q_{ext}	M_{sil}/M_{amc}	
0.6	0.56	2.61	0.0583	0.58	0.08	5.37	
0.6	0.56	2.61	4.00	0.56	2.18	13.0	
3.5	0.62	2.21	0.0641	0.64	0.10	0.65	
3.5	0.62	2.21	1.020	0.63	2.15	0.49	
3.5	0.62	2.21	1.376	0.62	2.35	0.61	

4.3.8 Modelling large masses of dust at early epochs: comparison with the results of Dwek & Arendt (2015)

In a recent analysis of infrared SED data, Dwek & Arendt (2015) (hereafter DA15) suggested that it may be possible for a large mass ($0.4 M_\odot$) of MgSiO_3 silicate dust to have been present in SN 1987A even at relatively early epochs ($t \sim 615$ days), since that species has very low IR emissivities. Up to this point I have constructed models using Zubko et al. (1996) BE amorphous carbon dust but in the previous section I discussed the effect on derived dust masses of instead using Draine & Lee (1984) astronomical silicate, which has higher optical and IR emissivities than the glassy MgSiO_3 species considered by DA15.

I now consider models for day 714 based on the grain types used by DA15. I adopt a clumped structure equivalent to the preferred model of DA15 who considered 1000 clumps with a filling factor of 0.09 and a negligible dust mass in the inter-clump medium. I calculate the effective spherical radius of my clumps by equating the volume of my cubic clumps to a sphere of radius R_{eff} . Clumps of width $R_{out}/14$ generate the desired $R_{eff}/R_{out} = 0.044$ equivalent to that of DA15. In my code, using a filling factor of 0.09 then generates 1034 clumps, similar to the number used by DA15. I ran a series of models (presented in Figures 4.19 and 4.20) for both the $\text{H}\alpha$ and $[\text{O I}]\lambda 6300, 6363$ Å line profiles. In each case I modelled the lines using a dust grain mixture as described by DA15 such that the medium comprised 18% amorphous carbon and 82% MgSiO_3 by volume. I adopted the same optical constants as used in their work (i.e. Jäger et al. (2003) for MgSiO_3 grains and Zubko et al. (1996) for amorphous carbon) and the same grain mass densities as DA15, $\rho_s = 3.2 \text{ g cm}^{-3}$ and $\rho_c = 1.8 \text{ g cm}^{-3}$. In addition to modelling their composite grain

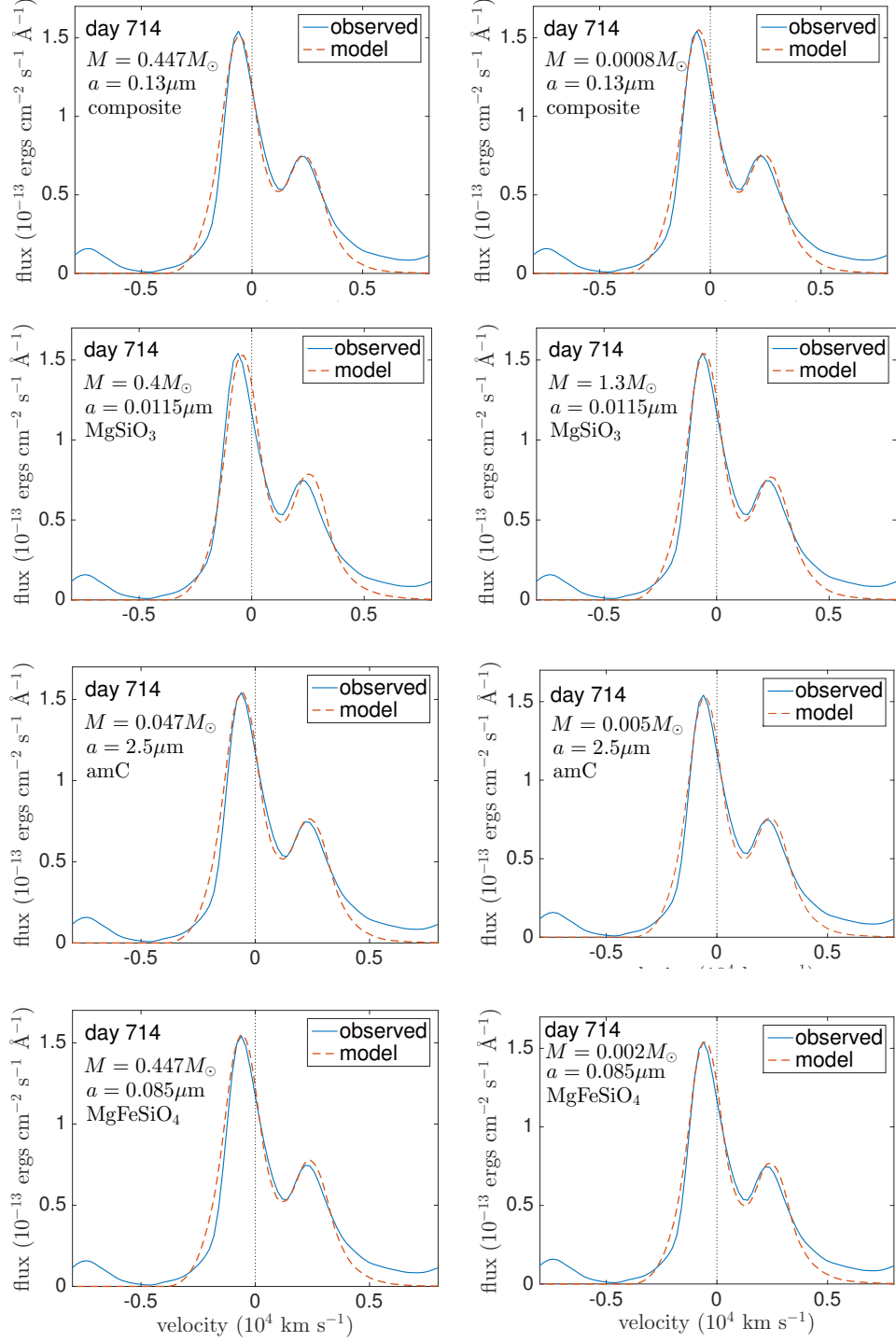


Figure 4.20. $[\text{O I}]\lambda 6300,6363 \text{\AA}$ models using different grain species and dust masses. Models using the dust masses presented by DA15 are on the top and models using my minimum required dust masses are on the bottom. From left to right the species are composite grains (82% MgSiO_3 and 18% amorphous carbon by volume), pure MgSiO_3 , pure amorphous carbon and pure MgFeSiO_4 . A density distribution with $\beta = 1.3$ was adopted with a filling factor $f = 0.09$ and an effective clump radius $R_{\text{eff}}/R_{\text{out}} = 0.044$. The ratio between the doublet components was 2.2. All other parameters are the same as in Table 4.5.

case, I also considered three single species models, using Zubko BE amorphous carbon, MgSiO_3 , and MgFeSiO_4 (in the latter two cases the optical constants were taken from Jäger et al. (1994) and Dorschner et al. (1995)). For each species I adopted the smallest single grain radius that has an albedo of $\omega \approx 0.6$. The ejecta parameters were as listed in Table 4.5, with the exception of the density distribution which I took to be $\rho(r) \propto r^{-1.3}$ for $\text{H}\alpha$ and $\rho(r) \propto r^{-2.3}$ for $[\text{O I}]$ in order to optimise the best fits.

For each species, two models are presented. The first adopts the minimum possible dust mass that provides a reasonable fit to the observed line profiles and the second uses the dust mass derived by DA15 for that specific species ($M = 0.4 M_\odot$ for MgSiO_3 and $M = 0.047 M_\odot$ for amorphous carbon giving a total composite dust mass of $M = 0.447 M_\odot$). I treated MgFeSiO_4 as I do the composite grains and adopted a dust mass of $M = 0.447 M_\odot$ for it. Results from the models are presented in Figures 4.19 and 4.20.

The $[\text{O I}]$ models can display similar profiles for substantially different dust masses. This is a result of the relatively high optical depths within the clumps themselves. If a clump is optically thick then the majority of radiation that hits it will be absorbed and the profile becomes insensitive to how much dust is actually contained within the clump. For my $[\text{O I}]$ minimum dust mass models, the optical depths within a clump over an effective clump radius R_{eff} at 6300Å are around $\tau_{clump} \approx 0.4$. Over the entire nebula optical depths are very high and $\sim 72\%$ of the total flux is absorbed. Increasing the total dust mass therefore has only a small effect on the emergent line profile and once $\tau_{clump} > 1$ then the line profile remains unchanged for increasingly large dust masses. It is because of this fact that I present only the smallest dust mass capable of reproducing the $[\text{O I}]$ profiles seen in Figure 4.20. The insensitivity of the $[\text{O I}]$ profiles to dust mass is not the case for the $\text{H}\alpha$ profile models (where $\tau_{clump} < 0.05$ for all of my models) and the $\text{H}\alpha$ -fit dust masses presented in Figure 4.19 therefore represent the most sensitive diagnostic of the dust mass for each grain type. All of my models discussed in previous sections have significantly smaller clump optical depths ($\tau_{clump} < 0.1$), making them sensitive to dust mass variations.

For all the $[\text{O I}]$ line profile models, except for those using pure MgSiO_3 or pure Mg_2SiO_4 dust, the required dust masses are significantly less than those proposed by DA15. The $[\text{O I}]$ profile obtained using DA15's very large MgSiO_3 dust mass of $0.4 M_\odot$ provides a reasonable fit, but the same dust mass significantly overestimates the blueshifting of the $\text{H}\alpha$ line (Figure 4.19). I can place an upper limit on the mass of pure MgSiO_3 on day 714

of $0.07 M_{\odot}$, as this is the highest mass for which a fit to the observed H α profile can be obtained (Figure 4.20).

Pure MgSiO₃ is extremely glassy, with very high albedos in the optical for a wide range of grain radii. At grain radii small enough to reduce the albedo to $\omega \approx 0.6$, in order to fit the observed line profiles, the extinction efficiency in the optical becomes extremely low (see Figure 3.9), with large masses of dust therefore required in order to produce even a small amount of line absorption. However, for a given albedo, the extinction efficiencies increase by large factors if either carbon or iron is included in the grain. In the composite grain model the amorphous carbon component dominates the overall extinction due to its much larger extinction efficiency at small grain radii. Similarly, for MgFeSiO₄ (or Mg_{0.5}Fe_{0.5}SiO₃) grains the iron component leads to much larger optical and IR extinction efficiencies and much lower dust mass upper limits. If the dust that formed at early epochs contained some fraction of elements such as carbon, iron or aluminium, yielding ‘dirtier’ silicate grains or composite grains, then fits to the observed blue-shifted line profiles imply low dust masses. I conclude that for dust masses as large as $0.07 M_{\odot}$ to have been present in SN 1987A’s ejecta as early as days 600-1000 then the dust would have to have been formed of glassy pure magnesium silicates.

In order to be certain that there was no set of parameters for which a dust mass of $M = 0.447 M_{\odot}$ comprising 82% MgSiO₃ and 18% amorphous carbon by volume could result in a good fit, a thorough investigation of the variable parameters was performed. Having fixed the clump size, filling factor, dust mass and composition as per the values detailed above and in DA15, I varied the density profile (β) and grain radius a . Varying the maximum velocity and the ratio of the inner and outer radii was found to have little effect on the goodness of fit. The MSE for the H α profile presented in the upper left panel of Figure 4.19 was 0.599 (in units of 10^{-13} ergs cm $^{-2}$ s $^{-1}$). This was improved to 0.246 by increasing the grain radius to $a = 0.6 \mu\text{m}$ and the density profile exponent to $\beta = 1.5$, which represents the best fit that I could achieve using the values described by DA15 and a dust mass of $M = 0.447 M_{\odot}$. However, the overall best fit I obtain for this scenario (see the lower left panel of 4.19) used a dust mass of $M = 5 \times 10^{-4} M_{\odot}$ giving a MSE=0.0058, substantially improving the fit.

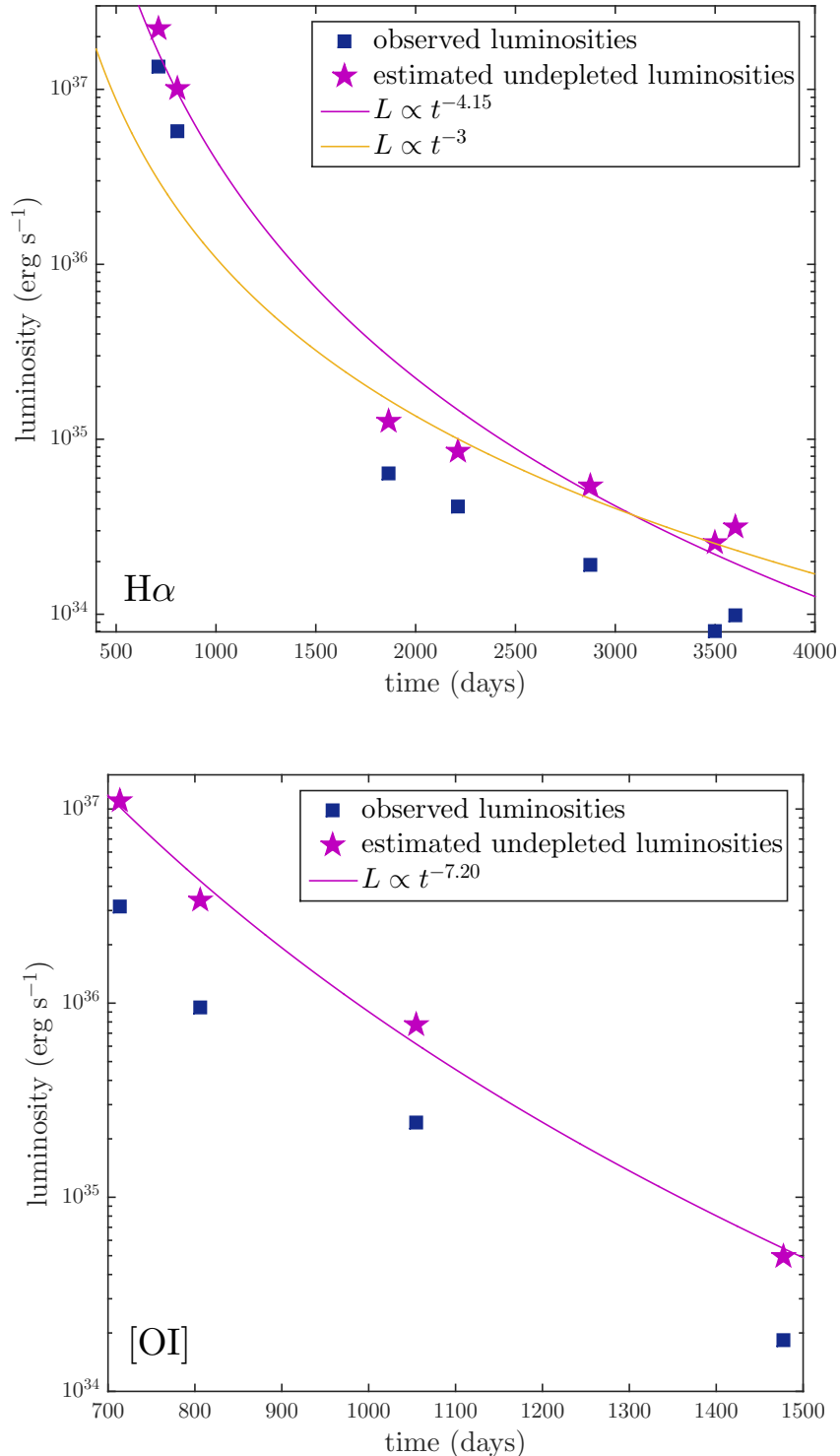


Figure 4.21. Predicted undepleted luminosities for the H α line (*above*) and [O I] $\lambda\lambda 6300, 6363$ Å doublet (*below*) presented with the best power-law fit to the data.

4.3.9 Unattenuated line fluxes

The evolution of the SN 1987A H α and [O I] $\lambda\lambda 6300, 6363$ Å line fluxes over time has been discussed previously by, for example, Li & McCray (1992), Xu et al. (1992) and Kozma & Fransson (1998b). I may use my clumped models to predict the unattenuated emitted line fluxes and consider their evolution through time. For each model, the fraction of the total line energy absorbed by the dust was predicted. I determined the total flux for each observed line profile and used the absorbed fraction from my clumped models for $a = 3.5\mu\text{m}$ to predict the undepleted flux of the line before attenuation by the dust. Gaps in the observed data due to contamination by narrow line emission were interpolated over in order to estimate the flux of the broad line component. The observed H α luminosities and predicted undepleted luminosities are given in Table 4.3 along with the energy fraction absorbed by the dust in each model. No correction has been made for interstellar extinction along the sightline to SN 1987A. There is very little change in these values if I adopt the models with $a = 0.6\mu\text{m}$ instead of $a = 3.5\mu\text{m}$. Plots of the observed and undepleted line luminosities are given for all modelled epochs of H α and [O I] in Figure 4.21.

I also present power-law fits to the time evolution of the unattenuated H α and [O I] line fluxes. For H α , I find that $L_{H\alpha}(t) \propto t^{-4.15}$ between days 714 and 3604. I can compare this value to the theoretical time dependence of the flux of a recombination line based on the dynamics of the ejecta for an environment in a Hubble-type flow $r = vt$. For a frozen-in ionization structure, the mean intensity of a recombination or collisionally-excited line per unit volume is locally proportional to the product of the densities of the recombining species i.e. $J_{H\alpha} \propto n_e n_p \propto n_e^2$. The total luminosity of the line is therefore dependent on the volume V as $L_{H\alpha} \propto 1/V$. Assuming a constant maximum expansion velocity, the luminosity should vary with time as $L_{H\alpha}(t) \propto t^{-3}$.

This relationship is only true for a constant ionization fraction. This “freeze-out” phase is estimated to have begun at ~ 800 days and first sets in at lower density high velocity regions, gradually moving inwards with time (Danziger et al. 1991b; Fransson & Kozma 1993). Since my modelling begins at day 714, the ionization fraction in the inner higher density regions is likely still decreasing due to recombination during my first two epochs. This presumably accounts for the slightly steeper $L_{H\alpha}(t) \propto t^{-4.15}$ that I find across all epochs. Kozma & Fransson (1998b) estimate that H α emission from the outer regions begins to dominate over H α emission from core regions for $t > 900$ days. If earlier

epochs are ignored, the last five epochs ($t \geq 1862$ days) plotted in (Figure 4.21) exhibit a shallower trend that is in good agreement with the expected $L_{H\alpha}(t) \propto t^{-3}$ evolution.

The $[O\ I]\lambda 6300, 6363$ Å doublet exhibits a much steeper evolution, $L_{[OI]}(t) \propto t^{-7.2}$, than the $H\alpha$ line (Figure 4.21). These collisionally excited lines are very sensitive to the gas temperature, with emissivities that fall to low values for temperatures below ~ 3000 K. The models of Li & McCray (1992); Kozma & Fransson (1998a) predict that the gas temperature in the relevant $[O\ I]$ emitting regions should have fallen below 1000 K after day ~ 1000 .

4.4 Discussion

Using Monte Carlo models that consider both the absorbing and scattering effects of dust, I have modelled the evolution of the $H\alpha$ and $[O\ I]\lambda 6300, 6363$ Å line profiles over time, enabling me to place constraints on the evolution of newly formed dust in the ejecta of SN 1987A.

As can be seen in Figure 4.12, even a small degree of asymmetry in observed supernova line profiles can be indicative of dust formation within the ejecta. In addition to this, a line profile that is consistently asymmetric through time requires increasingly large dust masses to account for a similar degree of blue-shifting since the expansion of the ejecta would otherwise cause the dust optical depth to the edge of the ejecta to be reduced.

In Section 4.3.8 I compared my results with those of Dwek & Arendt (2015) and concluded that large dust masses can only have been present at early epochs if the grains were formed purely of glassy magnesium silicates that contained no iron or carbon component and that even for pure magnesium silicates no more than $0.07 M_\odot$ can have been present. I now compare my results with those of Lucy et al. (1989) and W15.

Lucy et al. (1989) analysed the $[O\ I]\lambda 6300, 6363$ Å doublet for SN 1987A and estimated dust optical depths for a number of epochs. They translated these into dust masses for day 775 only. From my smooth flow modelling of the $[O\ I]$ doublets I obtain $\tau_V \approx 3.60$ at day 714 and $\tau_V \approx 2.86$ at day 806. These values are higher than the values given by Lucy et al. (1989) who derived $\tau_V = 1.19$ at day 725 and $\tau_V = 1.25$ at day 775. The value of the assumed albedo accounts for the majority of this discrepancy. Lucy et al. (1989) considered line profiles before and after dust condensation and concluded that any evidence of an extended red scattering wing was unconvincing. Accordingly, they adopted

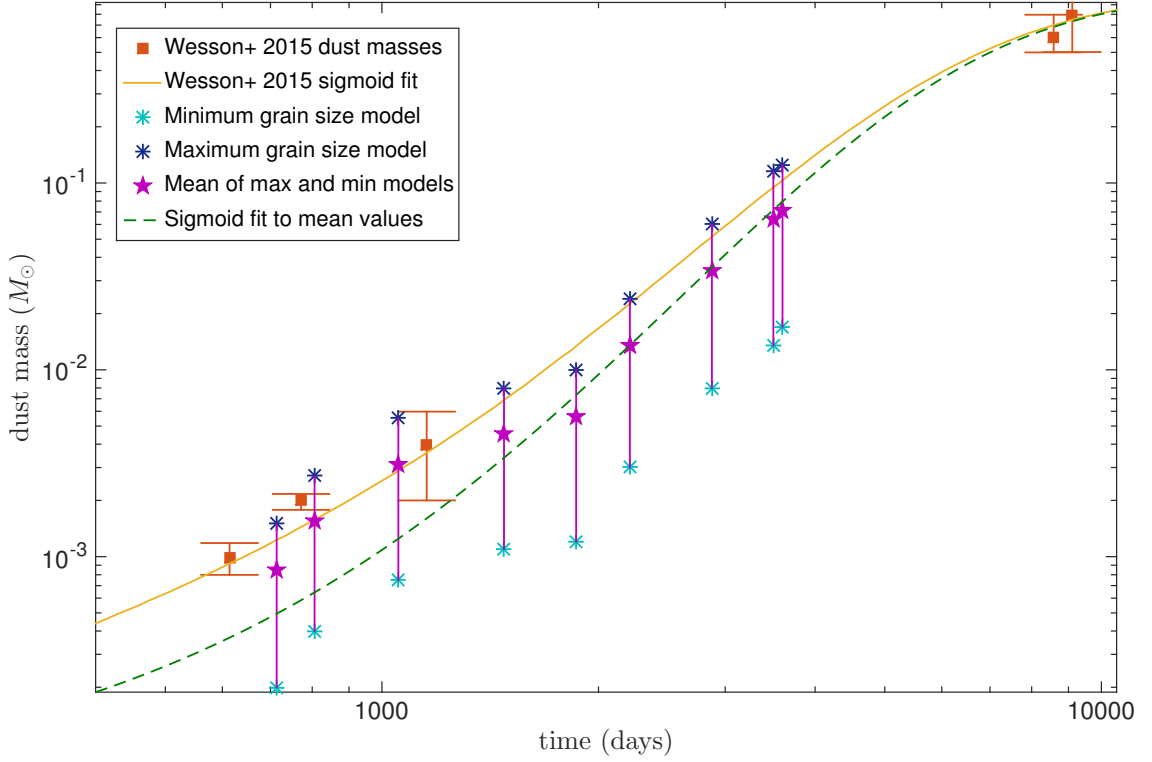


Figure 4.22. Derived dust masses for SN 1987A as a function of epoch. *Red squares* - dust masses derived by W15 from their photometric SED modelling of SN 1987A. *Yellow line* - W15's sigmoid fit to their values. *Dark and light blue asterisks* - maximum ($a = 3.5 \mu\text{m}$) and minimum ($a = 0.6 \mu\text{m}$) dust masses respectively for the [O I] models for $t \leq 1478$ days and for the H α models for $t \geq 1862$ days. *Purple stars* - predicted dust masses calculated as the mean of the maximum and minimum dust masses. *Green line* - sigmoid fit to my predicted dust masses.

a model with perfectly absorbing dust ($\omega = 0$). For my amorphous carbon models for the [O I] $\lambda 6300, 6363 \text{ \AA}$ profile using a grain radius $a = 0.35 \mu\text{m}$, I obtain an albedo of approximately $\omega = 0.5$ at $\lambda = 6300 \text{ \AA}$.

The dust masses derived by Lucy et al. (1989) at day 775 (e.g. $M_{dust} = 4.4 \times 10^{-6} M_\odot$ for amorphous carbon) are different to those obtained from my smooth dust modelling of the [O I] $\lambda 6300, 6363 \text{ \AA}$ doublet at day 806 ($M_{dust} = 1.5 \times 10^{-4} M_\odot$ for amorphous carbon). There are three main reasons for the discrepancy. Firstly, the albedo is significantly larger in my modelling as already discussed. A larger dust mass is therefore required to produce the same amount of absorption. Secondly, to match the extended red wing my required grain radius is considerably larger than the small grains ($a < 0.1 \mu\text{m}$) adopted by Lucy et al. (1989). Larger grain radii reduce the total cross-section of interaction and so a

greater dust mass must be present to compensate for this. Finally, the adopted maximum velocity (4000 km s^{-1}) in my model is larger than the value adopted by Lucy et al. (1989) (1870 km s^{-1}). The larger value of V_{max} increases the total volume of the ejecta significantly and therefore significantly more dust is required to produce the same optical depth.

Lucy et al. (1989) also noted that the dust optical depth increased rapidly after day 580 and that the rate of increase of the dust optical depth appeared to slow between day 670 and day 775, the latest day that they considered. My results, for both clumped and smooth models, suggest that the dust optical depth actually drops between day 714 and day 806 before starting to increase again at later epochs. This is consistent with the results of Lucy et al. (1989) where the slowing rate of increase of dust optical depth could be consistent with a turning point subsequent to day 775.

I can also compare my dust masses with the mass estimates derived from SED-fitting by W15 (see Figure 4.22). W15 used a sigmoid fit to their dust mass evolution, of the form

$$M_d(t) = ae^{be^{ct}} \quad (4.2)$$

where $a = 1.0M_\odot$ (representing the limiting dust mass), $b = -8.53$ and $c = -0.0004$. Both their dust masses and this sigmoid fit are shown in Figure 4.22. It exhibits an initial period of slow growth in mass followed by an intermediate period of accelerating growth followed by another slowing until a plateau is ultimately reached. In this sense it may be representative of the process of dust formation whereby initial conditions appropriate for grain growth gradually develop until optimal conditions are reached at an intermediate epoch when grain growth is at its fastest before conditions once again deteriorate and the rate slows again (as discussed by W15). Performing a least-squares regression to this function using just my own derived clumped dust masses, I obtain a sigmoid fit with coefficients $a = 1.0M_\odot$, $b = -10.0$ and $c = -0.0004$. These values are remarkably similar to those derived by W15. This sigmoid fit is also plotted in Figure 4.22.

I find that at all epochs the dust masses derived by W15 are entirely within the dust mass ranges determined by my models.

My sigmoid fit to the mean of the maximum and minimum dust masses does not take into account any systematic effects of grain growth. At earlier epochs, whilst grains are

still small relative to later epochs, the lower bound to the dust mass estimates may be more representative than the upper end; the reverse would be true at later epochs. This is in contrast to the sigmoid fit of W15, whose fits to their early epoch SEDs used an MRN distribution with grain radii between $0.005 \mu\text{m}$ and $0.25 \mu\text{m}$, whilst their fits to their last two epochs required grain radii between $3.005 \mu\text{m}$ and $3.25 \mu\text{m}$. The dust masses used for their sigmoid fit thus accounted for the effects of grain growth between the earlier and later epochs. As mentioned, I could not fit the extended red wings of the profiles at early epochs using an MRN distribution. W15 found that at their earlier epochs they could not obtain SED fits with grain radii as large as $\sim 1.0 \mu\text{m}$. However, they did not consider radii in between these size ranges, such as the grains with $a \approx 0.6 \mu\text{m}$ that I require at earlier epochs. For SED modelling it is generally the case that the larger the grain radius used, the less dust is required to produce the same level of flux. This may account for the differences between W15's earlier epoch dust masses and my own minimum dust mass estimates at similar epochs. The models of W15 used 15% silicate dust, in contrast to my models which used 100% amorphous carbon dust. This could also contribute to the differences at early epochs, as could the use of different sets of optical constants - I used the BE amorphous carbon optical constants of Zubko et al. (1996) whereas W15 used AC constants from Hanner (1988). W15 found that in order to fit early epoch SEDs epochs (e.g. day 615) with Zubko ACH2 constants, smaller inner and outer ejecta radii were needed, with half as much dust ($5.0 \times 10^{-4} M_{\odot}$) compared to the Hanner AC results.

W15 derived a maximum possible grain radius at late epochs, concluding that the grains could not be larger than $\sim 5 \mu\text{m}$ by day 8515. This is consistent with the maximum grain radii that I derive at my latest epochs. I find that grain radii most likely cannot have exceeded $\sim 3.5 \mu\text{m}$ at day 3604 - the dust mass that I obtain using this grain radius is similar to the value predicted by W15's sigmoid fit at that epoch.

The relationship between ejecta dust grain radii and post-explosion time is important for understanding the likelihood of dust surviving the passage of a reverse shock propagating back through the ejecta. By the time the effects of a reverse shock begin to appear in the line profiles (around day 5000), my models imply that the grains could already be as large as several microns in radius and are likely to be larger than $\sim 0.6 \mu\text{m}$. Grains as large as this are more likely to survive destruction by sputtering in supernova reverse shocks and in interstellar shocks (Silvia et al. 2010, 2012; Slavin et al. 2015). It has been suggested that very large grains (radii up to $4.2 \mu\text{m}$) formed in the ejecta of SN 2010jl

within a few hundred days after the explosion Gall et al. (2014). The grain radii that W15 and I obtain for SN 1987A at very late epochs are nearly as large as found by Gall et al. (2014) for SN 2010jl, with both results suggesting that grains large enough to survive the destructive force of a reverse shock have formed by a few hundred days post-explosion.

The dust masses obtained from my modelling of SN 1987A’s line profiles support the conclusion of W15 that even after ~ 3000 days the dust mass was still only a fraction of its current value. This contrasts with the results of Sarangi & Cherchneff (2015) whose grain chemistry models predict that ejecta dust masses should plateau by around 5 years after the explosion. My results show that SN 1987A’s dust mass had reached the order of $0.1M_{\odot}$ by day 3604. Since its present dust mass is several times larger than this (Matsuura et al. (2015), W15), a substantial fraction of the current dust mass must have condensed after this epoch, in agreement with the conclusions of W15.

Ideally, my models would cover the entire evolution of SN 1987A’s H α line profiles up to the present day. However, the excitation of gas in the outer edges of the ejecta by the reverse shock after \sim day 5000 results in significant broad and asymmetric emission that dominates the original line profile (Fransson et al. 2013). In addition to this, the narrow lines from the ER start to become so strong relative to the declining broad H α profile that, post-removal, not enough of the broad profile remained to be able to reliably infer information from the profile structure. These factors may be common to some other CCSNe that have interactions with surrounding circumstellar material. Care should also be taken to ensure that any observed late-time line profiles being modelled are not in fact the product of a light echo reflecting the spectrum from near maximum light. Nonetheless, detailed line modelling of asymmetric line profiles has proved effective in determining dust masses in the ejecta of SN 1987A at multiple epochs during the first ten years after outburst. The method clearly has wider application to other supernovae as demonstrated in Chapter 5.

4.5 Conclusions

I have modelled the H α and [O I] $\lambda 6300, 6363$ Å line profiles from SN 1987A over a range of epochs and have obtained dust masses of the order of $0.1M_{\odot}$ by day 3604. I derive a sigmoid fit to my dust mass data that predicts a current dust mass of $0.68M_{\odot}$, in line with current SED-based dust mass estimates for SN 1987A. I find that large grains are

necessary in order to reproduce both the extended red scattering wings and the asymmetry seen in several of the lines and that grains larger than $0.6 \mu\text{m}$ have formed by day 714, while by day 3604 grain radii of $\sim 3.5 \mu\text{m}$ are needed. I find from fits to the H α profile that dust masses cannot have exceeded a few $\times 10^{-3} M_{\odot}$ on day 714 for all the grain types investigated, apart from glassy pure magnesium silicate grains, for which up to $0.07 M_{\odot}$ can be fitted.

The observed red-blue line asymmetries persist right through to day 3604 and beyond - if no further dust had formed after day ~ 800 then the expansion of the ejecta dust shell would cause dust optical depths to drop rapidly with time thereafter, leading to the disappearance of red-blue asymmetries. Just to maintain the observed degree of red-blue asymmetry seen at the earlier epochs therefore requires that dust must have continued to form beyond those epochs.